Università degli Studi di Pavia

Dipartimento di Fisica

Corso di Laurea Magistrale in Fisica

Neutron autoradiography track counting algorithm for BNCT: calibration and evaluation through a Geant4 Monte Carlo simulation.

MSc thesis by:
Samir El Bouadli

Supervisor:
Prof. Ian Postuma

A.A. 2023-2024

Abstract

La Boron Neutron Capture Therapy (BNCT) è un trattamento oncologico avanzato che sfrutta l'interazione tra neutroni di bassa energia e boro-10 per colpire selettivamente le cellule tumorali. Il principio alla base della BNCT è la reazione nucleare in cui i neutroni termici vengono catturati dal boro-10, provocando l'emissione di particelle ad alto trasferimento lineare di energia (LET), ovvero particelle alfa e nuclei di litio. Queste particelle inducono danni letali a livello cellulare, in particolare nelle zone in cui il boro è maggiormente concentrato, risparmiando invece i tessuti con una bassa concentrazione di boro. Pertanto, se il boro si accumula selettivamente nel tumore, la BNCT può distruggere le cellule tumorali senza danneggiare quelle sane circostanti. Con la progressiva attivazione di impianti BNCT a livello globale, rimangono sfide cruciali come l'ottimizzazione della somministrazione di farmaci contenenti boro, la valutazione accurata della deposizione di dose e il miglioramento della selettività tumorale.

Un aspetto chiave della ricerca sulla BNCT è lo sviluppo di vettori di boro più efficaci, capaci di migliorare l'assorbimento tumorale riducendo al contempo la tossicità sistemica. Gli studi preclinici svolgono un ruolo fondamentale nella valutazione della biodistribuzione, concentrazione e localizzazione microscopica del boro nei tessuti biologici. La capacità di quantificare con precisione la concentrazione di boro nei siti tumorali è essenziale per valutare l'efficacia di nuovi composti, ottimizzare i protocolli terapeutici e migliorare gli esiti clinici dei pazienti.

In questo studio, abbiamo utilizzato rivelatori a traccia nucleare a stato solido, in particolare il CR-39, per quantificare la concentrazione di boro nei campioni tumorali. Il CR-39 registra le tracce lasciate dalle particelle cariche risultanti dalle reazioni di cattura neutronica, permettendo l'imaging diretto e la quantificazione del danno da radiazione indotto dal boro. Per automatizzare e migliorare l'analisi delle tracce, ho sviluppato un algoritmo di elaborazione delle immagini in Python utilizzando OpenCV, in grado di rilevare e contare in modo efficiente le tracce lasciate dalle particelle nelle immagini al microscopio dei rivelatori CR-39 irradiati. Questo approccio automatizzato garantisce un'elevata accuratezza e riproducibilità nelle misure di concentrazione del boro.

Inoltre, ho progettato e implementato una simulazione Monte Carlo utilizzando il toolkit Geant4 per perfezionare la metodologia di conteggio delle tracce. Questa simulazione modella il processo di irraggiamento, tenendo conto delle interazioni neutroniche all'interno del campione tissutale e dell'emissione dei prodotti di reazione. Un risultato cruciale di

questa simulazione è la stima dell'efficienza geometrica, ovvero la probabilità che le particelle generate all'interno del campione tissutale raggiungano con successo il rivelatore. Integrando questo fattore di efficienza, colmiamo il divario tra i conteggi sperimentali delle tracce e le previsioni teoriche, consentendo una valutazione più accurata della concentrazione di boro nei campioni biologici.

Questo approccio combinato sperimentale e computazionale fornisce un metodo per assistere lo sviluppo di nuovi farmaci BNCT, offrendo uno strumento prezioso per studi preclinici futuri volti allo sviluppo di composti a base di boro più efficaci. In definitiva, il nostro lavoro contribuisce a migliorare l'efficacia della BNCT affinando le tecniche dosimetriche e approfondendo la comprensione della distribuzione del boro nei tessuti biologici.

Abstract

Boron Neutron Capture Therapy (BNCT) is an advanced oncological treatment that uses the interaction between low-energy neutrons and boron-10 to selectively target tumor cells. The principle behind BNCT is the nuclear reaction in which thermal neutrons are captured by boron-10, leading to the emission of high linear energy transfer (LET) particles, namely alpha particles and lithium nuclei. These particles induce lethal damage at cellular level, particularly where boron concentrates, while sparing tissues with low boron concentration. Thus, if boron concentrates in tumor, BNCT can selectively destroy tumor cells without harming surrounding healthy cells. As BNCT facilities become operational worldwide, a crucial challenge remains: optimizing boron-containing drug delivery, accurately assessing dose deposition, and improving tumor selectivity.

A key aspect of BNCT research is the development of more effective boron carriers that enhance tumor uptake while reducing systemic toxicity. Pre-clinical studies play a pivotal role in evaluating the biodistribution, concentration, and microscopic localization of boron in biological tissues. The ability to precisely quantify boron concentration in tumor sites is fundamental for assessing the effectiveness of new compounds, optimizing treatment protocols, and improving patient outcomes.

In this study, we employed solid-state nuclear track detectors, specifically CR-39, to quantify boron concentration in tumor samples. CR-39 registers the tracks left by charged particles resulting from neutron capture reactions, enabling direct imaging and quantification of boron-induced radiation damage. To automate and enhance track analysis, I developed a Python-based image processing algorithm using OpenCV, which efficiently detects and counts particle tracks in microscope images of the irradiated CR-39 detectors. This automated approach ensures high accuracy and reproducibility in boron concentration measurements.

Additionally, I designed and implemented a Monte Carlo simulation using the Geant4 toolkit to refine our track-counting methodology. This simulation models the irradiation process, accounting for neutron interactions within the tissue sample and the subsequent emission of reaction products. A crucial outcome of this simulation is the estimation of the geometric efficiency (i.e., the probability that particles generated within the tissue sample successfully reach the detector). By incorporating this efficiency factor, we bridge the gap between experimental track counts and theoretical predictions, allowing for a more accurate evaluation of boron concentration in biological samples.

This combined experimental and computational framework provides a robust method for assisting BNCT drug delivery strategies, offering a valuable tool for future pre-clinical studies aimed at developing more effective boron-containing compounds. Ultimately, our approach contributes to improve BNCT treatment efficacy by refining dosimetry techniques and advancing the understanding of boron distribution in biological tissues.

Contents

Introduction

Boron Neutron Capture Therapy (BNCT) is an advanced form of radiation therapy that exploits the nuclear reaction between boron-10 (^{10}B) and thermal neutrons to selectively destroy cancer cells while sparing surrounding healthy tissue. The principle of BNCT relies on administering a boron-containing compound that preferentially accumulates in tumor cells. When the tumor is then exposed to a thermal neutron beam, the ^{10}B(n,α)^{7}Li reaction occurs, releasing high linear energy transfer (LET) particles (i.e. alpha (α) particles and lithium (^{7}Li) ions). These charged particles have a very short range (approximately 5–9 μm), meaning their destructive effect is confined to the cancer cells where boron has accumulated, minimizing collateral damage to surrounding healthy tissue.

Despite its promise, the clinical effectiveness of BNCT is highly dependent on the selective uptake and retention of boron in tumor cells while minimizing its presence in normal tissues. To date, only two boron containing compounds (i.e. sodium borocaptate (BSH) and boronophenylalanine (BPA)) have been approved for clinical BNCT applications. However, extensive research is ongoing to identify new boron carriers with improved selectivity and efficacy.

A pivotal aspect of BNCT research is the quantification of boron uptake microscopic distribution and concentration in tumor cells. The ability to accurately measure the boron distribution within cells is critical for evaluating the effectiveness of the boron delivery agents and ensuring optimal neutron irradiation conditions. This is true in clinical and preclinical studies.

How to measure boron in biological samples

One of the methods measure boron in solid and liquid samples is neutron autoradiography, a technique that exploits the properties of the boron-neutron capture reaction to map boron distribution at a microscopic and macroscopic level [1, 2].

Neutron autoradiography is based on the interaction of ^{10}B with thermal neutrons, resulting in the emission of high-LET α particles and lithium ^{7}Li ions. When a boron containing tissue sample is coupled to a solid state nuclear track detector (SSNTD) and then irradiated with a neutron beam, charged particles, from the boron neutron capture reaction, are emitted in all directions within the tissue sample. Consequently, some alpha and lithium ions may reach the surface of the tissue sample and strike the detector.

One of the materials used in neutron autoradiography is polycarbonate or CR-39 plastic. Upon impact, these particles leave permanent microscopic damage tracks in the detector material which are not visible by eye or light microscopy (i.e. latent tracks). The location and density of these tracks is correlated to the distribution of boron within the tissue.

After neutron exposure, the CR-39 detector has to undergo a chemical etching process to enlarge the radiation induced tracks, making them visible under an optical microscope. The number of tracks per unit area is proportional to the local boron concentration, enabling quantitative analysis. To further refine the evaluation of this technique, Monte Carlo (MC) simulation can be used to evaluate the detection efficiency, ensuring a more precise estimation of the boron content in the sample.

Neutron autoradiography is used in preclinical studies and it is particularly important in the evaluation of the performance of new boron compounds, as it provides a high-resolution, quantitative assessment of boron distribution in biological tissues and/or cells. This information is then used to evaluate the cell survival as a function of the dose, which can be computed appropriately using the information on boron concentration as the input. [3].

Structure of this work

This work aims at optimizing a counting algorithm for the tracks obtained in the CR-39 detectors and at verifying the results by Monte Carlo simulations.

In the first chapter, we start by introducing the concept of BNCT. The rationale of the technique will be briefly explained, covering the physical mechanisms. We will underline the advantages of BNCT as compared to older radiological techniques and a description of the technology currently available to sustain the clinical applications will follow. Particular attention will be given to the explanation of how neutrons are generated to be used in BNCT facilities and how the neutron beam is obtained and adapted to the clinical necessities. Then, neutron autoradiography will be explained with particular attention to its role in our work. We will show how we applied this technique to biological samples and we will report some examples of the tracks so obtained on the CR-39 plates. In the following chapter, a more detailed description of interaction processes between neutrons and high-LET particles (focusing particularly on α particles and Li ions) with matter will be described. There, some common reactions that occur during BNCT treatments are recalled in more detail, also focusing on problems deriving from such interactions, such as dose delivery outside the tumor to healthy tissues. In the last part of this work, we will walk through the codes. We will start with the tracks counting algorithm. We will show in detail every process carried out, from the initial image manipulation, that prepares the input images so that the tracks revelation will be more efficient, to the effective tracks counting. After that, we will proceed with the Monte Carlo simulation by Geant4 transport code. This simulation was meant to evaluate the reliability of the boron concentration obtained with the counting algorithm. In fact, this simulation calculates the percentage of α particles that hit the CR-39 compared to the total generated in the sample, enabling a validation of the counting algorithm. A brief conclusion chapter

will end the work, containing considerations and findings regarding the potential of this technique in the research and development of new boron carriers for BNCT.

Chapter 1

Boron Neutron Capture Therapy

This chapter will cover the relevant part of BNCT to the scope of this dissertation. Though, before describing what BNCT is and how it can be applied, a brief introduction to the intaraction of radiation with matter is necessary.

1.1 High-LET ionising radiation

Ionising radiation has been used in medicine for decades. However, for the majority of time, only X-Rays or protons (in more recent years) were used in treatments. It was already known that α particles and other heavier nuclei were better in damaging tumors tissues [4] (they have a higher RBE, which will be introduced later). Despite of that, we only recently achieved an adequate technological level to properly use them as a treatment. Using charged nuclei instead of the typical X-Rays guaranties different benefits. First of all, differently from photons, alpha particles and other nuclei are electrically charged. That offers the possibility to accelerate them, using accelerators, while also actively select their trajectory. Furthermore, their range in matter is related to their energy. Hence, by setting the appropriate energy, charged particles can deliver dose in precise points. As a consequence, proton therapy or carbon therapy proved to be more precise in avoiding normal tissue while targeting tumors [5]. That's true even if a charged particle beam is delivered from outside the body. In fact, the following equation, known as the Bethe-Block equation, represents the amount of energy deposited in the infinitesimal length, along the x axis, from a charged particle of charge z_e moving at speed v in a material with atomic number Z and density ρ.

$$S = -\frac{dE}{dx} = \frac{4\pi e^4 z_e^2}{m_e v^2} \rho Z \left[\ln\left(\frac{2m_e v^2}{I}\right) - \ln\left(1 - \frac{v^2}{c^2}\right) - \frac{v^2}{c^2} \right] \tag{1.1}$$

Where the letter "S" stands for stopping power, which is equal to the energy loss ratio per unit length. As it is visible from a direct inspection of this formula, a charged particle loses, per unit length, much more energy if it moves at low speeds. The direct

consequence of this fact is that, if the energy loss is plotted against the reached dept in a specific material, we obtain what is called the Bragg peak (a characteristic curve with a peak at its end), after which the incident particle is absorbed or stopped due to lack of energy. An example of that is shown in the figure 1.1. Here we notice how the majority of the particle energy is released deep in the tissues (if we are considering the radiation beam to hit a patient), at around $4cm$ of depth, while shallow tissue receive just a fraction of the total energy, being preserved from potential damages. This is the opposite of X-Rays which in contrast deposit the majority of their energy in the first centimeters of their path, after a brief build-up region, in the patient body. While it passes through the patient, the X-Ray beam (considered as monochromatic in this case for simplicity) is attenuated exponentially, following the equation:

$$I = I_0 e^{-\mu x} \tag{1.2}$$

with I_0 the initial intensity of the beam, and μ the linear attenuation coefficient (which depends on photon energy and material). The intensity I of the radiation beam in this case doesn't depend on the particle speed as in equation 1.1, but only from the reached depth x. Another relevant feature of the Bragg peak is that there is the possibility to shift its depth (and consequently the tissue volume receiving the higher dose/energy) by simply adjusting the entrance energy of the radiation particles: the more energetic the incident particles are the deeper they will go and vice versa. That allows to target a tumor with more precision in all its extension, assuming its position is known thanks to previous investigations. However, in this condition, it is still impossible to completely avoid dose to those tissues located along the entry path. As anticipated, in BNCT charged particles are generated inside tumor cells. α and Li particles obtained from ^{10}B neutron capture have an energy such that their Bragg peak happens in a range similar to the cell dimension. That is the reason behind the high selectivity of this technique: particles derived from BNCT treatment aren't able to directly irradiate surrounding tissues and the majority of the energy carried is transferred to the tumor only. Obviously, this happens as long as the difference in boron concentration obtained with a particular compound between healthy and tumor tissues is broad. And here comes the necessity to develop better and better drugs for clinical treatment.

The Bragg peak reported in figure 1.1 is different in case it was obtained using heavier nuclei than alpha particles (oxygen, carbon...). That is due to the fact that those said particles could undergo a fragmentation process while interacting with other particles, generating smaller nuclei (such as alpha particles). Fragmentation is a problem generally regarding radiotherapy performed with heavy nuclei (such as C) and its absence in BNCT represent another advantage of this technique. In fact, from equation 1.1 we notice that the energy loss is proportional to the particle number Z. Fragmenting, the resulting particles have a lower Z and that implies a reduction in the energy loss rate. As a consequence, those resulting particles can proceed deeper in the tissues, delivering dose in regions which were not meant to be irradiated. This phenomenon becomes more relevant as we use more and more massive particles and should be taken into account.

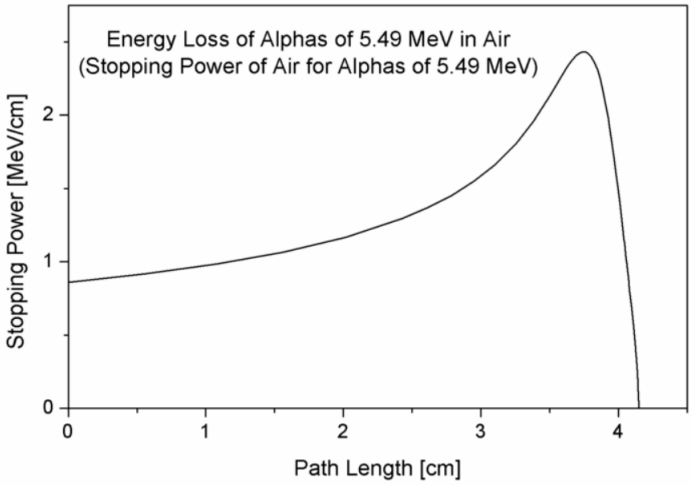

Figure 1.1: Bragg peak for alpha particles. [5]

By a graphical point of view it can be observed with the appearance of a "tail" at the end of the Bragg peak, beyond the range of the primary particles.

Photos are able to better pass through obstacles and a photon beam requires a longer path to be absorbed than a alpha particles beam (or any other heavy nucleus) with the same initial energy. That feature can be observed by directly plotting equations 1.1 and 1.2 and retrieving the reached depth of both photons and charged particles in a chosen material. This is a consequence of the fact that heavy nuclei and alpha particles are densely ionising radiation. In other words, they manage to frequently interact with the surrounding environment (via electromagnetic interaction, and collisions) dispersing a higher amount of energy per unit length. That aspect can be formalised by introducing the concept of LET (Linear Energy Transfer). By a mathematical point of view LET is equal to the restricted collision stopping power, which is in turn the fraction of the collision stopping power where only secondary radiation under a certain cutoff (Δ) energy value is produced. Restricted collision stopping power and LET were introduced to account for dose overestimation if calculated with the Bethe-Block 1.1 formula or with the collision stopping power alone. In fact, a part of that energy could escape the mass targeted with the radiation if energetic enough, under the form of secondary radiation (electrons or gamma rays). A dose (energy deposited per unit mass) calculation using the Bethe-Block would than return a too high value, keeping into account all the escaped radiation which deposited its energy somewhere else. Restricted collision stopping power solves that problem by not taking into account those particles whose energy is above a particular level which would allow them to escape the target mass.

$$L_\Delta = \left(\frac{dE}{dx}\right)_{c,\Delta} \tag{1.3}$$

If we wanted to take into account all the secondary particles produced by the interaction

without any restriction than the LET would be equal to the collision stopping power. As already mentioned LET is a parameter that allows to gives a glimpse on how rapidly radiation transfer its energy to the surrounding environment. LET becomes higher in value as the mass of the involved particles (the ones composing the radiation beam) increases (if we consider ions with the same energy per nucleon). For this reason heavy nuclei will create a bigger biological damage (same energy lost by in a smaller volume) and will be more effective in killing cancerous cells when irradiated. The difference in the biological damage produced by different type of radiations can be parameterised by another quantity, know as RBE or Relative Biological Effectiveness. In particular RBE is a ratio between the damage produced by a determinate type of radiation per unit of energy deposited in a biological tissue and the damage produced (in the same tissue per unit of energy deposited) by the γ-ray radiation obtained from the decay of cobalt-60 nuclei (generally used as reference radiation) or other high-energy photons [6]. Despite its simple definition RBE is an extremely variable and complicated quantity: its value is function of the radiation type, cell or tissue variety and dose [7]. RBE is directly evaluated from the count of single or double strand breaks (SSB or DSB) reported at a microscopic level, in the DNA structure caused by the rupture of the bonds between the molecules due to ionization induced by the passage of the radiation, or other macroscopic endpoints. It is relevant to underline that RBE and LET are interconnected: a higher LET implies a greater energy loss which could lead to more biological damage [8], or similarly, a higher count of SSB or DSB in a DNA sample. However, as shown in the image 1.2 below, the SSB and DSB count is a function of LET which doesn't follow a linear correlation. As we can see there's a peak in the damage yield at a certain LET value (equals for all the different ions) with a subsequent decline. This trend repeats itself indiscriminately if we valuate the SSB, DSB or clusters (more SSB or DSB in the same region of DNA) counts.

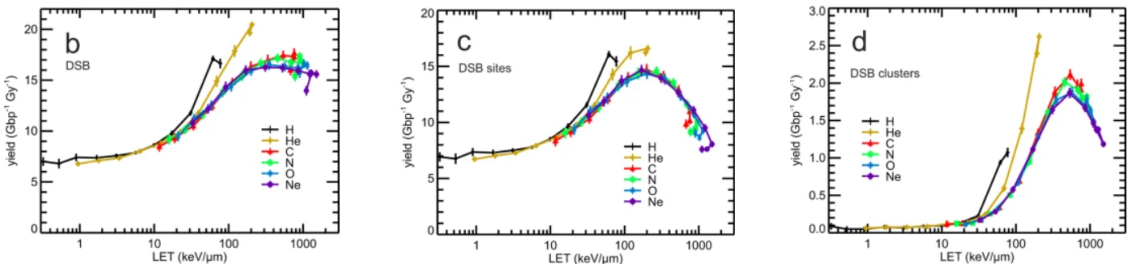

(a) DSB yields (b) Yields of DSB sites (c) Yields of DSB clusters

Figure 1.2: Ion irradiation-induced DNA damage in dependence on LET [8].

Coming back to the RBE, it is important to note that the value of the RBE is determined by a ratio. So, it reflects both the changes in effectiveness of the high- and low-LET radiation taken in the examination. The effects of low-LET reference radiation, in particular, could be highly modified by different factors at low doses, and thus the RBE value must be carefully contextualized. In addition, data related to the high-LET radiation interaction with humans is limited to some alpha emitters. For other particles, such as neutrons, it is still necessary to rely on a experimental approach for its determination [7]. BNCT

effectiveness relies on the usage of high-LET, and thus high-RBE, nuclei which can cause great damage in a limited volume. The presence of DNA in proximity of the boron capture point guarantees a high probability of interaction between the charged particle and the genetic material, with a consequently low probability of cell survival.

1.2 Neutron radiation

Together with high-LET ionising radiation the other important element in BNCT is neutron radiation. First of all neutron don't have any significant electrical charge. They do not directly ionise matter but lose their energy via scattering, elastic or inelastic collisions and capture processes (such as in BNCT); putting in motion other charged particles that will eventually ionise the surrounding atoms. In the elastic scattering the neutron hits a nucleus, transferring it part of its energy and changing its direction of movement. In this case the energy loss is linked to the difference in mass between the two involved particles (neutron and nucleus): the greater the difference the lower the energy transferred, as visible from equation 1.4. [9]

$$E_{tr} = E_n \frac{4MM_n}{(M + M_n)^2} \cos^2 \theta \tag{1.4}$$

In this equation E_n and M_n represent the initial energy of the neutron and its mass respectively, while M the target mass. As we can see the quantity E_{tr} depends on the scattering angle θ and it is greatest if the neutron hits the target head-on. As already mentioned targets whose masses are similar to the proton mass are more efficient in slowing down neutrons, for this reason materials which contain a larger amounts of hydrogen will be a better choice as a neutron screen or moderator. The elastic scattering cross-section is energy dependent with a non uniform trend. As visible in fig 1.3.

At higher energies neutron elastic cross sections becomes extremely variable, with narrow peaks immediately followed by deep decreases. Those resonances are a common aspect in neutron radiation and their presence must be taken into account when dealing with particular energy ranges. From equation 1.4 we see that H is thus particularly efficient in moderating neutrons and its wide presence in human body (water) is the reason of why we need an ephitermal neutron flux entering the body if we intend to treat a deep tumor, as explained in the first chapter.

Neutrons can interact via inelastic scattering too. In this case the target nucleus is brought in an excited state after the collision with the neutron (in order to promote a nucleus to an excited state the neutron energy must be greater than a threshold value characteristic of each nucleus). It will come back to its ground state thanks to the emission of one or more γ-rays or another neutron such that $E_{n'} < E_n$ ($E_{n'}$ is the energy of the newly released neutron). Such produced gamma rays pose a serious radiation hazard due to their high energy and consequently an enhanced penetration ability. An example of such a reaction is the collision between a neutron and a ^{16}O nucleus that brigs the latter into an excited state, $^{16}O^*$, from which a 6.1 MeV γ-ray will be produced [9].

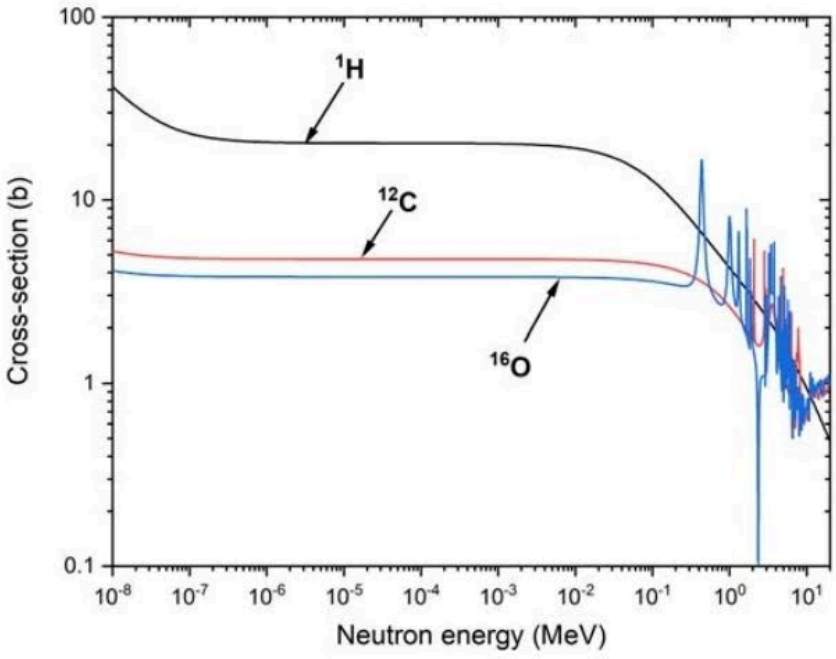

Figure 1.3: Neutron elastic scattering cross-section from the Korea Atomic Energy Research Institute (KAERI) evaluated data library. Above approximately 2 MeV, the ^{16}O and ^{12}C cross-sections exhibith sharp increases and decreases (resonances) [10].

In some cases the incoming neutron could form a compound nucleus in an excited state that later decays emitting a particle. An example of that it is again the neutron capture from oxygen nuclei where a Carbon nucleus and an α particle can be produced ($^{16}O(n,\alpha)^{13}C$). It must be noted that the produced particles could be in an excited state and an emission of γ-rays could follow. This phenomenon takes places at high energies (ranging from few MeV to 10 MeV). For this reason it doesn't generally represent a big problem in BNCT treatments which make use of low energy neutrons. However, potential fast neutron contamination of the beam could give rise to this scenarios. That's why processes of filtration and moderation are extremely important.

Similarly, neutrons which have undergone different scattering processes (and have reached the thermal region) could be absorbed by a nucleus too. In this case an isotope can be formed, as in the case of the deuteron, whith the possibility of γ-rays to be released. Differently, as it happens for BNCT, we have the formation of secondary particles ($^{10}B(n,\alpha)^{7}Li$), with a disintegration similar to the one mentioned before, but that takes place at lower energies. Other kinds of interactions, such as the fission process, won't be of our interest and won't be treated in this work. What is relevant is that neutrons have the ability to "activate" matter. As previously said an inelastic interaction could lead to excited states in nuclei that will later emit some kind of radiation to come back to their ground state. It can happen that, if the neutrons interact with some metals, those excited states have half-lives of minutes or even hours. This means that there could be

the possibility to have potentially hazardous residual radiation, even after the primary neutron beam is extinguished [9].

In the previous chapter we introduced equation 1.2 that shows how photons are attenuated in matter. Neutrons and photons are both uncharged particles, therefore they share the same behavior when referring to attenuation, so even a neutron beam intensity decreases exponentially in matter. That requires the use of thick screens when trying to attenuate neutrons as they can travel a lot in matter before being absorbed. In the case of a human body, which is largely composed of water, thus of hydrogen, neutron-proton scattering is extremely frequent, especially at low energies. In particular, for a fluence of neutrons Φ, of energy E, we can write the Kerma as [9]:

$$K = \frac{dE_{tr}}{dm} = \Phi E \frac{\mu_{tr}}{\rho} \qquad K = \int \Phi E \frac{\mu_{tr}}{\rho}\, dE \tag{1.5}$$

The former used in the case of monochromatic radiation, the latter if the neutrons energies are distributed. If equilibrium of charged particles is established, Kerma is equal to dose.

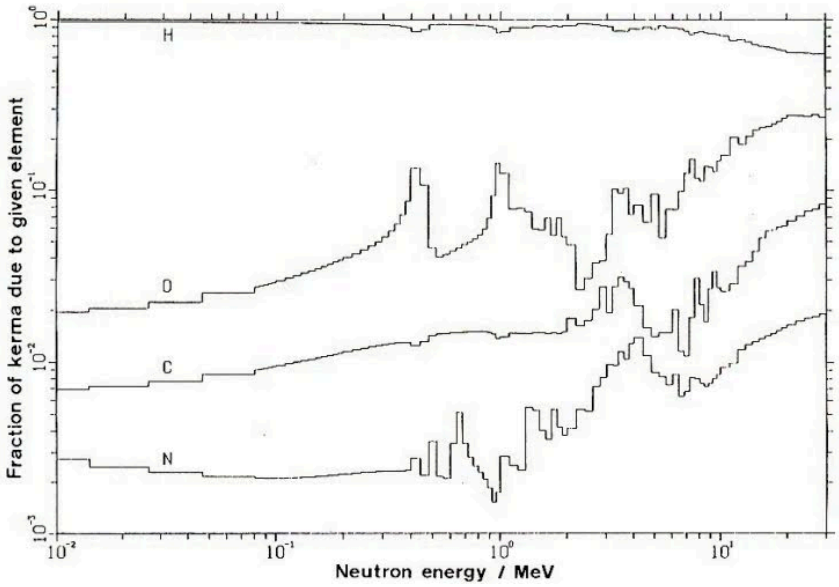

Figure 1.4: Fast neutron relative contributions to Kerma for ICRU tissue from interactions between neutrons and H, C, O and N [11].

In figure 1.4 it is possible to observe the fraction of the total Kerma due to different kind of interactions as function of the neutron energy (in an ICRU phantom). As it is clearly visible the vast majority of energy deposited in form of Kerma derives from the neutron-proton (H nuclei) scattering processes, despite hydrogen only accounts for 10% of the total body mass. In particular, at low energies, the cross-section for hydrogen-proton interaction increases (see figure 1.3) and the Kerma so produced accounts for about 90% of the total. That percentage tend to decrease while the neutron energy grows and the

contribution from O, C and N increases. It is extremely relevant to note that neutrons, while interacting with matter, generate secondary radiation which is composed of both photons and charged particles. For this reason neutrons produce a mixed radiation field where particles with different RBE coexist. In particular, RBE for neutrons varies a lot. As indicated in the previous chapter RBE is energy dependent, and in this specific case the ICRP indicates a value ranging from 5 to 20, with some uncertainties for very low and very high energies. Neutrons' RBE shows a peak for intermediate energies while decreases for low and high ones [7].

1.3 Introduction to BNCT

The concept of BNCT was first proposed in 1936 and it is based on the fact that a ^{10}B nucleus is able to capture a thermal neutrons with an high cross section, see Figure 1.5. This reaction generates an α particle and a recoil ^{7}Li nucleus, which in 94% of the times is generated on an excited level promptly decaying by releasing a photon of 478 keV. The two charged particles have high Linear Energy Transfer (LET) and are emitted back to back. In biological tissue, the combined range of these particles is similar to the cell dimension (12-13 μm). Thus, this reaction releases approximately 2.8 MeV and 2.3 Mev respectively in 6% and 94% of the cases limited to the cells containing boron and their first neighbors. In principle, if only tumor cells uptake boron, the therapy will selectively kill only those cells. The main advantage of BNCT is thus its ability to deliver high dose to microscopically selected targets which is not possible with other radiation therapies. In BNCT the selectivity is achieved thanks to the fact that ^{10}B is delivered to the tumor using a drug. By adjusting the time elapsed between the administration and the irradiation, it is possible to maximize the concentration ratio between the tumor and the normal tissue. Also, thanks to that selectivity, only tissues around the tumor absorb a significant dose, while other are better preserved than in other radiation therapy techniques [12, 13]. BNCT can be described as an *internal hadrontherapy* as the biological effect is caused by a charged particles whose Bragg peak occurs in the cell where the charged particles has been generated.

In order to be effective in relatively short irradiation times, BNCT requires the generation of an intense neutron flux. It is necessary to obtain a thermal flux (Maxwellian distribution with an average of 0.025 eV) at the depth of the tumor to trigger the ^{10}B capture process with maximum probability. For this reason, an epithermal flux (energies distrbuted between 0.5 eV and 10 keV) is required at the entrance in patience, as neutrons will be moderated while they penetrate through the body (processes of neutron interaction with matter are better explained in the following chapter). To better visualize this fact, we can compare the thermal neutron flux obtained at specific depths in the two scenarios of thermal and epithermal neutron beams irradiating a tissue volume (Figure 1.6). As shown, a thermal flux at the entry point is significantly attenuated in few centimeters and for this reason it could not be used to treat deep-seated tumors. Thus, clinical neutron beams for BNCT are characterized by an epithermal spectrum to allow for a deeper penetration in the body.

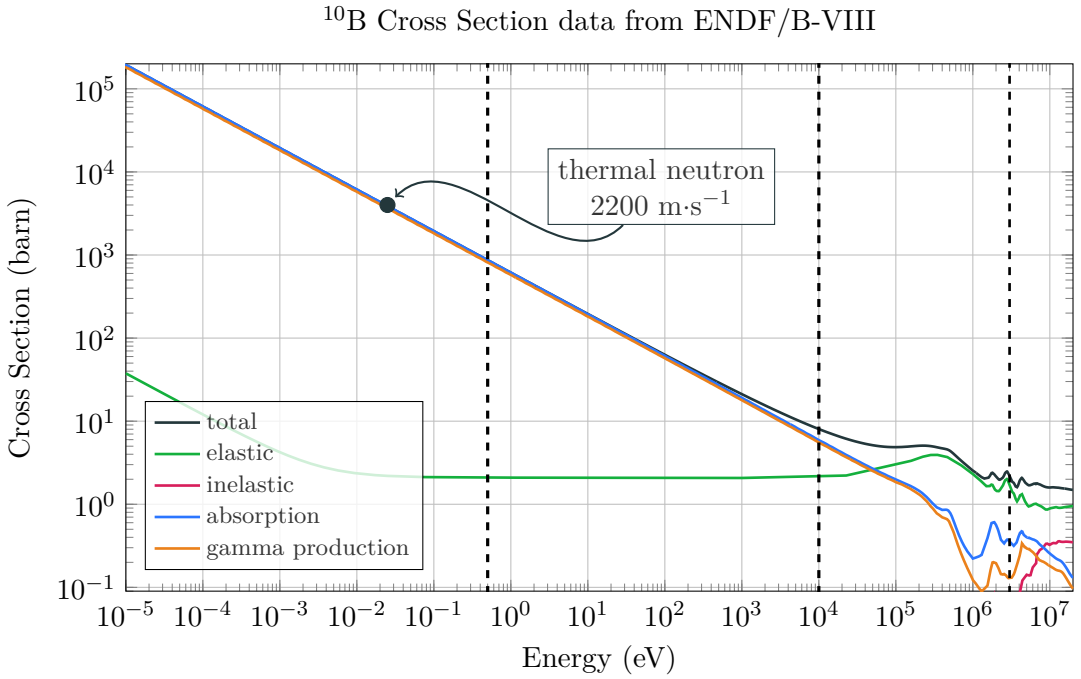

Figure 1.5: Cross sections for the neutron reactions in boron-10. At thermal neutron energies (i.e. 25 meV, approximately equal to 2200 m·s^{-1}) the thermal neutron cross section is 3738 barn. The dotted vertical lines represent different neutron energy limits. The line at 0.5 eV separates thermal from epithermal neutrons, at 10 keV the line separates epithermal from fast neutrons. These limits are the conventional classification of neutrons according to their energy. The vertical line at 3 MeV is the maximum energy of a neutron spectrum generated by 5 MeV protons on a Be target.

A desirable minimum beam intensity, as in the IAEA guidelines for BNCT, is 10^9 neutrons cm^{-2} s^{-1} at the tumor site. Lower fluxes (in the order of 10^8) could be used, but this would require longer irradiation times to deposit the same dose [12]. On the other hand, the quality of the spectral characteristics of the beam are another important factor: γ and fast neutron contamination could be detrimental for the treatment because they are a source of non-selective dose deposition. This would limit the dose deposition in the tumor because the tolerance dose in surrounding healthy tissue would be reached in shorter time. A beam diameter of around 10-15 centimeters (or larger for some extended tumor regions) should be used, in order to fully irradiate the tumor volume [13].

A particularly relevant aspect in BNCT is the calculation of the dose deposited in the patient. Differently from photon radiotherapy, where the radiation field in the patient is composed secondary electrons are produced, in this case a wide variety of radiation types coexist because of neutron interaction with the different elements in the biological tissues. In addition to the capture reaction in ^{10}B, the most relevant neutron interactions are with ^{1}H and ^{14}N, which capture thermal neutrons with consequent release of charged particles and γ-rays. In particular the reaction $^{1}H(\mathrm{n},\gamma)^{2}H$ produces 2.2 MeV photons and the

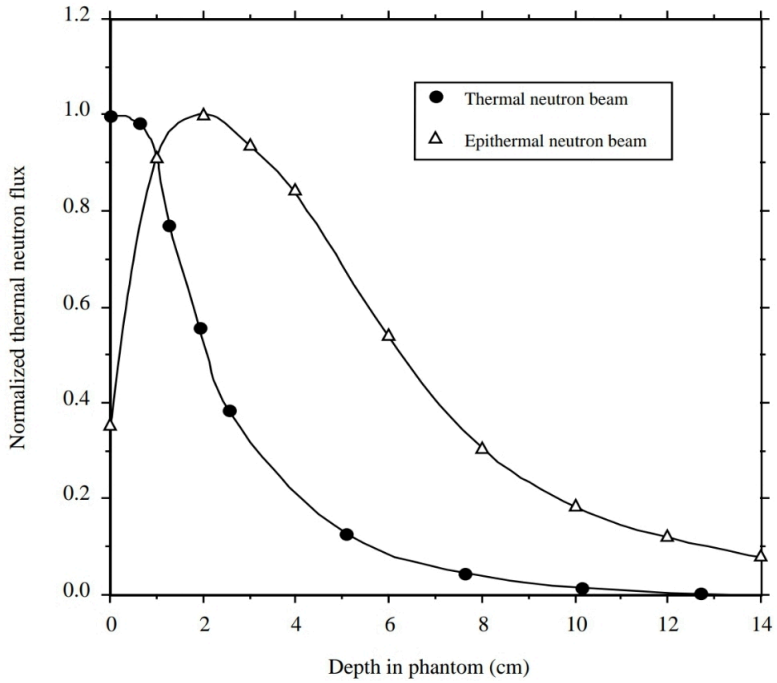

Figure 1.6: Intensity of the thermal neutron flux as a function of depth, in the cases of thermal and epithermal neutron beams irradiating biological tissue [12].

reaction ^{14}N(n,p)^{14}C produces protons of 580 keV. Moreover, the isotopes ^{1}H, ^{14}N and ^{12}C are responsible for elastic collisions that occur with more energetic neutrons [13]. Figure 1.7 shows the relevant contributions to the dose by plotting the kerma factors for neutrons going from 10−5 to 10^7 eV, which is the common neutron energy range for BNCT.

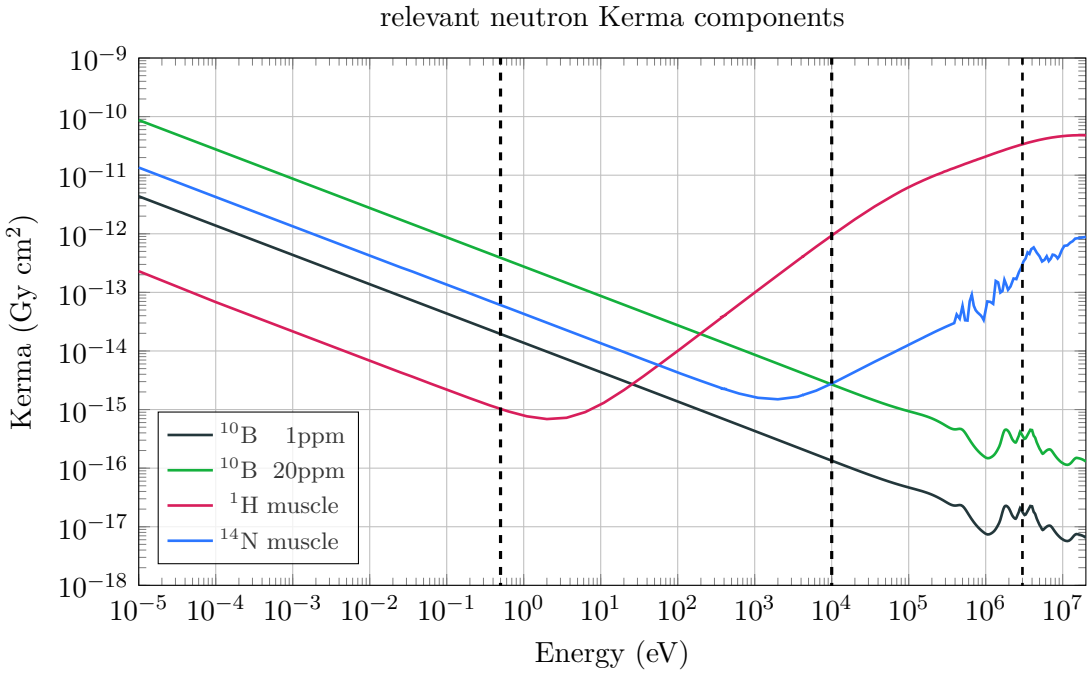

Figure 1.7: Relevant kerma factors for radiation components in BNCT. As shown, for thermal neutron energies, a boron-10 concentration of 20 parts per million (ppm) in tissue is sufficient to make the boron neutron capture component dominant. For higher energies the scattering on hydrogen becomes the most important, especially true for fast neutron. This is why the fast component in the clinical neutron spectrum must be reduced as much as possible.

1.4 Neutron radiation sources

For many years, nuclear reactors were the only neutron sources capable of delivering the high flux required for Boron Neutron Capture Therapy. However, these reactors were designed primarily for research, not for clinical applications. As a result, BNCT treatments were limited to specialized research facilities, often located far from hospitals, making accessibility a significant challenge and limiting the organization of large clinical trials.

To be effective for BNCT, the neutron beam must be carefully filtered and moderated. Nuclear reactors primarily generate fast neutrons, which have high kinetic energy and are unsuitable for BNCT. Through a process called moderation, these fast neutrons are slowed down to the desired thermal (below 0.5 eV) or epithermal (0.5 eV – 10 keV) energy ranges, which are optimal for boron capture in tissues. Moderation is achieved using materials such as graphite, heavy water, or aluminum and lithium fluoride, which scatter and reduce the energy of the neutrons without significantly absorbing them. Essentially, low Z materials which do not significantly absorb neutrons are used to moderate high energy neutrons towards the epithermal energy range. However, neutron capture in some

typical materials also generates secondary gamma contamination. Moreover, a certain gamma contamination is related to the fission process in the reactor core. All together, a gamma contamination is unavoidable in the neutron beams, and it should be reduced as much as possible by appropriately designed gamma filters, such as high Z materials like lead or bismuth.

While reactor-based neutron sources have demonstrated the clinical potential of BNCT, the need for a more accessible, hospital-compatible alternative has driven the development of accelerator-based neutron sources (ABNS). These modern systems generate neutrons through nuclear reactions induced by proton or deuteron beams striking a target of lithium or beryllium. Accelerator-based sources offer greater flexibility, improved safety, and the potential for widespread clinical implementation of BNCT. Accelerators, in fact, are machine relatively small, that can be hosted into hospital, and that do not require the complex authorization procedures needed for the installation of a nuclear research reactors. They are easy to be operated and maintained and do not raise any acceptability issues. Thus, the possibility to operate these machines, makes it possible to transfer BNCT into clinical environments and to start modern clinical trials.

Neutron spectra generated by ABNS contain less energetic neutrons and the process of beam shaping and moderation is simpler. For ^7Li targets, the proton reaction producing neutrons has a threshold energy of 1.88 MeV [12] and its cross-section shows a resonance of 580 mb at 2.25 MeV [14]. In this scenario, neutrons are emitted predominantly in the same direction as the incident proton beam, thus the neutron beam is already well collimated and with an average energy slightly higher than the required epithermal BNCT spectrum. Thus, this reaction is a good choice for ABNS because moderation and collimation needed is mild, which maintains a high neutron flux. However, there are some technical difficulties regarding the stability of the target and its usage: first of all ^7Li produces ^7Be by proton capture, which is radioactive and emits γ-rays of 477 KeV. This poses a radiation protection problem when the target must be decommissioned or it must be extracted for maintenance. Moreover, ^7Li is reactive with oxygen, becoming explosive, for this reason the target plate needs to be encapsulated. Finally, the high current of protons (of the order of 10 mA) required to obtain an acceptable flux of neutrons deposits a high power in Li, which can be easily melted. The cooling of the Li target is thus a very important technological aspect. On the other hand, ^9Be targets have the advantages of avoiding activation and resisting better to the heat generated by the power dissipated by the proton beam. However, this advantage comes with a higher threshold energy respect to ^7Li. This fact has the consequence to generate a neutron flux which is intrinsically more energetic than the one generated in the first case. For this reason, more moderation and filtering are required. Also, Be has low permeability of H (protons), causing the formation of hydrogen bubbles inside the target when it is thick compared to the range of proton in Be (blistering). Blistering ruins the target and requires frequent changes. This fact can be overcome by producing thin Be targets, so protons that are not captured can exit the target without forming the bubble. In general, Be poses technological issues that are easier to be faced especially considering its use in hospital-based facilities, also considering the lack of γ radiation due to activation. The $^9Be(p,n)^9B$ reaction requires

4-5 MeV bombarding protons in order to obtain a sufficient yield, and higher proton currents (order of 30 mA). Also in this case, thus, a proper cooling of the target is required.

At present, nuclear reactors are still widely used neutron sources. The University of Pavia, in the LENA laboratory, hosts a TRIGA Mark II reactor, used for research purposes. This reactor has a thermal column, consisting in a horizontal block of moderating graphite, that has been modified in the Eighties to obtain an irradiation position characterized by a uniform field of thermal neutrons. The facility consists of an air channel (dimensions: 1 m by 40 cm by 10 cm) in which samples can be inserted to be exposed to a high thermal neutron flux (from $10^{10}\ cm^{-2}\ s^{-1}$ in the position closest to the reactor core to $10^{9}\ cm^{-2}\ s^{-1}$ at its entrance). Figure 1.8 shows a simulated model of the reactor and its thermal column.

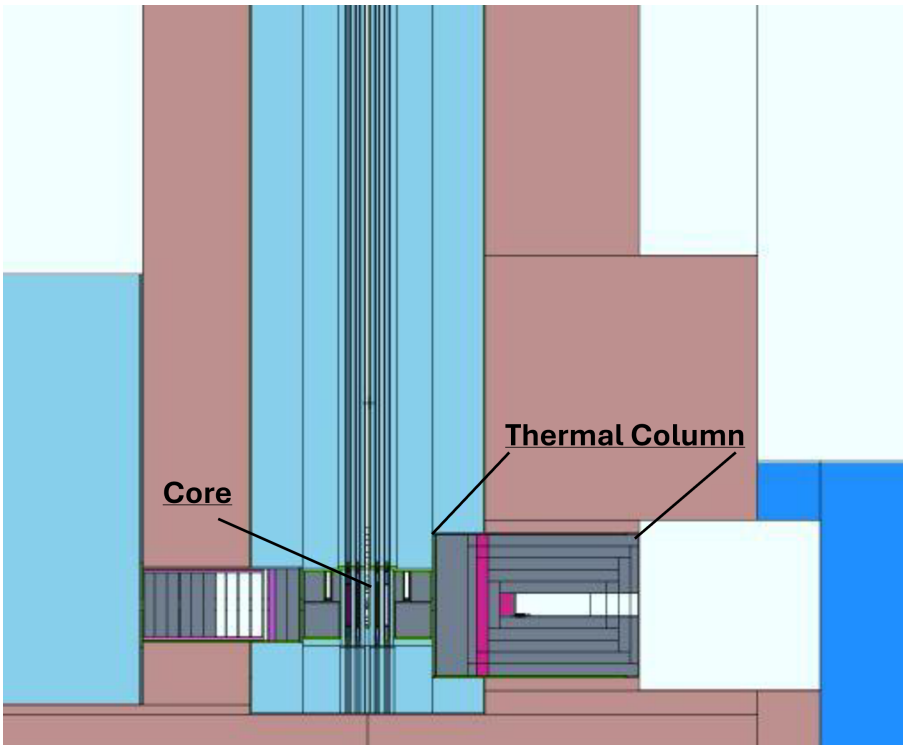

Figure 1.8: Simulation model of the TRIGA Mark II reactor of the University of Pavia. The vertical section shows the reactor core immersed in water (light blue) and the thermal column with the graphite depicted in gray and the air channel in white.

1.5 Boron measurements in preclinical studies

Measuring boron in preclinical studies of BNCT is crucial for evaluating the biodistribution of boron containing compounds, ensuring effective tumor targeting, and minimizing toxicity to healthy tissues. Moreover, a precise knowledge of boron concentration in tissues allows for a robust dosimetry calculation. Various analytical techniques are used to

quantify boron concentration in biological samples, including blood, tissues, and water solutions. Below an overview of the main methods employed to measure boron concentration is provided [15]. Methods that are only employed in clinical practice were excluded in the following description, which rather focuses on the techniques used to quantify boron in radiobiological models.

1.5.1 Inductively Coupled Plasma Mass Spectrometry

Inductively Coupled Plasma Mass Spectrometry (ICP-MS) is a technique that uses a high temperature plasma source to ionize the sample, followed by mass spectrometric detection. It is widely used in BNCT due to its excellent sensitivity and precision. Since, to be effective, BNCT needs a concentration of about 20 parts per million the main advantages of ICP-MS is its high sensitivity, it can detect parts per billion (in mass) of a certain isotope. The main disadvantages of this technique is that it requires a costly specialized equipment and that it can be affected by contamination and matrix effects. In BNCT ICP-MS is used in clinical practice to measure boron concentration in blood, tumor, and normal [15].

1.5.2 Inductively Coupled Plasma Atomic Emission Spectroscopy

Inductively Coupled Plasma Atomic Emission Spectroscopy (ICP-AES), also known as Inductively Coupled Plasma Optical Emission Spectroscopy (ICP-OES), is used in BNCT for quantifying boron concentrations in biological samples. While ICP-MS (Inductively Coupled Plasma Mass Spectrometry) is often preferred due to its higher sensitivity, ICP-AES remains a valuable tool, especially when high throughput and robustness are needed. ICP-AES uses a high-temperature argon plasma ($\approx$ 10,000 K) to excite atoms in a sample, causing them to emit light with characteristic wavelengths. The intensity of the emitted light is proportional to the concentration of the element in the sample. For boron measurement in BNCT studies, the emission wavelengths typically used are around 249.7 nm and 208.9 nm [15].

1.5.3 Prompt Gamma Neutron Activation Analysis

Prompt Gamma Neutron Activation Analysis (PGNAA) exploits the fact that the neutron capture reaction, in 93% of the cases, leaves the lithium ion in an excited state, emitting a characteristic prompt gamma ray (478 keV). This can be detected using a high-purity germanium (HPGe) detector. This technique is a direct and non-destructive measurement of boron-10; it requires a thermal neutron source (e.g., a research reactor or accelerator), low gamma background, and it has a lower sensitivity compared to ICP-MS. PGNAA is used in BNCT to directly measure boron-10 concentration in tissues and organs often in preclinical small animal studies [15].

1.5.4 Neutron Autoradiography

Neutron autoradiography (NA) will be covered more extensively in Chapter 2 because it is the main topic of this thesis work. Generally this technique is applied to a thin tissue

section which is exposed to thermal neutrons. During the irradiation boron-10 captures neutrons to produce alpha particles and lithium nuclei. These particles leave tracks in nuclear emulsion films or CR-39 detectors, which can be visualized and analyzed after the irradiation. This technique can be applied at various scales, thus it provides spatial distribution of boron in tissue at a macroscopic and microscopic level. Like PGNAA, neutron autoradiography requires thermal neutron irradiation. Furthermore it is labor intensive and time consuming. Anyhow it is a relatively simple and low-cost technique and its main advantage is the possibility to obtain information of boron bio-distribution besides average boron concentration values. Neutron autoradiography is thus used in preclinical studies to assess the heterogeneity of boron distribution and concentration at a cellular and subcellular level [15].

1.5.5 Time-of-Flight Secondary Ion Mass Spectrometry

Time-of-Flight Secondary Ion Mass Spectrometry (ToF-SIMS) uses a focused ion beam to desorb and ionize boron-containing molecules from tissue surfaces, allowing for high-resolution imaging of boron distribution. Consequently, it has an high spatial resolution (sub-micrometer) and it can provide molecular information about boron compounds. Anyhow, it requires extensive sample preparation and it is limited to surface analysis. in BNCT ToF-SIMS has been used to visualize boron uptake in tumors and surrounding tissues at a subcellular level [15].

1.5.6 Fluorescence and Raman Spectroscopy

Some boron compounds can be labeled with fluorescent or Raman-active molecules, allowing for non-invasive imaging of boron biodistribution. This technique has the advantage of being non-destructive and it allows real-time imaging in living tissues. The limitation is that not all boron compounds are fluorescent, for example, the main borated drugs used in clinical practice (i.e. BPA and BSH) are not. This technique is thus interesting only for a class of formulations with certain optical characteristics. Furthermore, the quantification of boron concentration has a lower accuracy. This technique is used for *in-vitro* imaging of boron biodistribution in preclinical models [15].

1.5.7 Summary

Depending on the type of information needed for the preclinical research, there are several boron concentration measurement techniques available. Table 1.1 contains a summary of the main advantages and disadvantages of these techniques. For the activity carried out in Pavia, we will focus on neutron autoradiography, which is appropriately tuned in the parameters of the neutron fluence and etching solution and time, to obtain imaging and quantification of boron in samples. The details of this work will be described in the following chapter.

Technique	**Sensitivity**	**Accuracy**	**Advantages**	**Limitations**
ICP-MS	Very High (ppt)	Very High	Highest sensitivity, small sample volume	expensive, requires specialized lab
ICP-AES	Medium (ppb)	High	Robust, cost-effective, high throughput	mean boron concentration only
PGNAA	Medium (ppm)	High	Non-destructive	mean boron concentration only
NA	High (spatial, ppm)	High	Cheap, macro and micro resolution	Time consuming
ToF-SIMS	High (spatial, ppt)	High	Subcellular resolution	Surface analysis only
Fluorescence	Medium (spatial)	Low	*in-vivo* analysis	Not adequate for concentration measurements

Table 1.1: Summary of the available boron measuring techniques

Chapter 2

Neutron autoradiography

The effectiveness of BNCT relies especially on the delivery of an adequate amount of boron to cancer cells. Therefore, accurately measuring boron concentration is crucial for optimizing treatment protocols and ensuring effective tumor targeting while minimizing damage to surrounding healthy tissue. Neutron autoradiography helps in achieving this by providing a direct method to visualize and quantify boron uptake in tumors, also guiding the development of new boron carriers [16].

Neutron autoradiography involves irradiating a tissue or cell sample previously treated with a borated formulation in a low-energy neutron beam. This leads to the production of charged particles when boron nuclei capture neutrons. These charged particles can then be detected and mapped, creating an image that reflects the concentration and the position of boron nuclei within the sample. The technique is particularly valuable because it allows for non-destructive analysis, enabling the preservation of tissue integrity for further preclinical studies and to understand the biodistribution of the drug compared to the different structures of the tissue or the different compartments of a cell [17].

During neutron irradiation, various ionizing particles such as photons, electrons, positrons, protons, alpha particles, and heavy charged ions are generated. Consequently, the film serving as the detector must allow to recognize only the radiation of interest. A primary issue to consider in this technique is the sample thickness that can be analyzed, which depends on the range of the particles to be detected. However, this constraint can also be advantageous, as it eliminates the need for a collimated neutron beam. In fact, being the range of the charged particles emitted by neutron capture in boron very short, their path from the cells/tissues through the detector is not influenced by the direction of incoming neutrons. The thermal column of the TRIGA Mark II reactor provides an optimal facility for neutron autoradiography of biological samples, ensuring uniform exposure to a thermal neutron field.

Neutron autoradiography can be applied in different ways. In BNCT there are three techniques: *qualitative macroscopic distribution*, *quantitative macroscopic concentration* and *quantitative microscopic distribution and concentration*.

Qualitative boron uptake measurements, shown in Figure 2.1, rely on irradiation at high neutron fluence and limited etching times to enhance the visibility of the tracks produced by the alpha particles and lithium ions from the $^{10}B(n,\alpha)^{7}Li$ reaction. The entire sample is irradiated uniformly, ensuring a dense distribution of reaction events on the surface of the detector. The etching process, typically performed in a NaOH or KOH solution at elevated temperatures (e.g., 60–70°C), enlarges the tracks enough to be observed using a standard optical or digital microscope without additional magnification. The tracks overlap forming a map of different optical density which is proportional to boron concentration. In this way, it is possible to obtain the imaging of bio-distribution of boron in the sample itself. If the sample is a section of tumor tissue, for example, it is possible to compare the map of boron distribution with the histological preparation of a subsequent section. Different types of tissues into the tumor (active metabolic cells, fibrotic areas, necrosis, remaining normal tissues) will uptake different boron concentrations and these differences can be appreciated in the spatial map of neutron autoradiography. To capture macroscopic images of the boron distribution, a high-resolution scanner or a low-magnification stereomicroscope equipped with a digital camera is used. The field of view typically ranges between 30 and 50 mm^2, allowing for a broad visualization of how boron is distributed across the sample. The contrast in track density provides qualitative insights into the heterogeneity of boron uptake. Image processing software may be employed to enhance track visibility and map boron-rich regions.

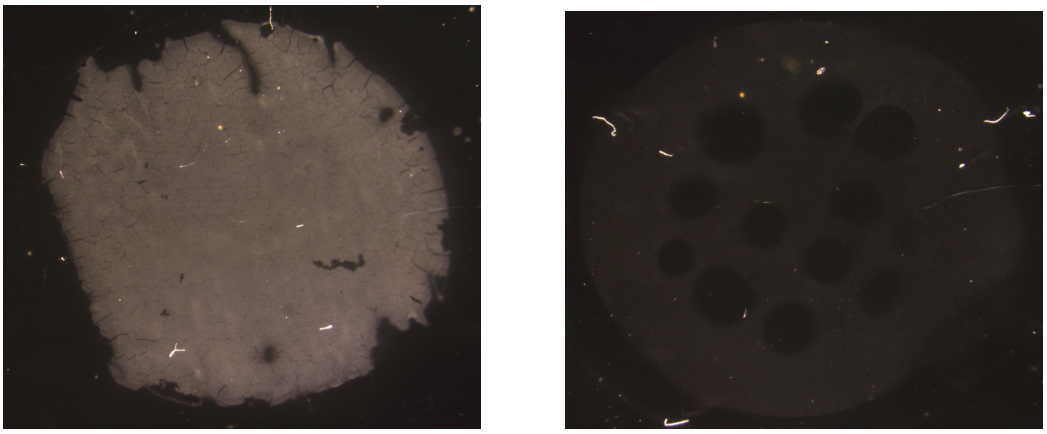

(a) (b)

Figure 2.1: Qualitative observation of boron concentration in two tissue samples. The autoradiography of image 2.1a has an higher contrast with respect to image 2.1b. This increase of gray scale level is proportional to the amount of tracks in the sample. Therefore, the sample relative to image 2.1a has an higher boron content with respect to the sample of 2.1b.

For precise measurements of boron concentration quantitative autoradiography can be performed. In this case, the sample undergoes irradiation at a much lower neutron fluence to prevent track overlap, ensuring an accurate counting because the tracks remain

separated and recognizable. After irradiation, the sample is subjected to a controlled etching process of shorter duration, optimizing track clarity while maintaining their original density. Microscopic images are captured using a high-magnification optical microscope (e.g., 40× to 100× objective) equipped with a digital camera. The field of view in this case is much smaller, typically around 0.3 mm^2, allowing for detailed visualization of the tracks, Figure 2.2 shows a typical quantitative image with tracks. Image analysis software (such as ImageJ or custom-developed algorithms) is then used to count the number of tracks per unit area. A calibration curve, obtained from reference samples with known boron concentrations, enables the conversion of superficial track density into absolute ^{10}B concentration values. This method ensures quantitative accuracy and it is critical for precise dose estimation in boron neutron capture therapy studies.

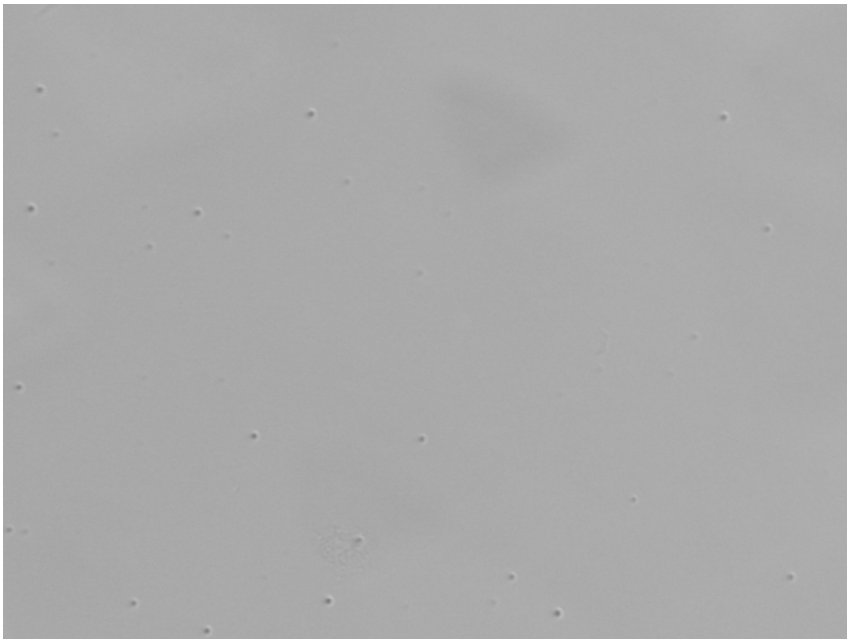

Figure 2.2: Microscopic image of tracks left by α particles and lithium ions on a CR39.

2.1 Neutron autoradiography set-up at LENA

Boron uptake measurements are obtained with neutron autoradiography, by irradiating cell/tissue or liquid samples in the thermal column of the TRIGA MARK II nuclear reactor at LENA. Detectors are then treated by chemical etching in a PEW or NaOH solutions, respectively for quantitative and qualitative measurements. The etching develops the characteristic alpha/lithium latent tracks that can be visualized through a microscope. Finally, average boron concentration in the sample is obtained by transforming track density, using the appropriate calibration curve, into ^{10}B concentration. In the following section each of these steps are described.

2.1.1 Materials

The materials necessary to perform neutron autoradiography to quantify boron with the quantitative approach are:

- **Detector**: Solid State Nuclear Track Detector (SSNTD). We use CR-39, the trademark name of poly-allyl-diglycol-carbonate (C12H18O7). Its most important characteristic is that it is not sensitive to photons, thus they can be used in ambient light without being damaged. CR-39 are used to detected only high-LET charged particles, allowing to avoid the detection of the background.
- **Microscope**: Leica M205 FA
- **Stage**: Prio OptiScan II
- **Software**: ImagePro plus (version 7.0)
- **Etching Solution**: PEW40

2.1.2 Irradiation

The sample preparation is the first step of the procedure. Biological sample adequately fixed (i.e. dry tissue sections or cell pellets on Mylar support) are firmly positioned onto the CR39. The positioning procedure is described in [18]. If the sample is in liquid state, we use a proper holder, shown in Figure 2.3, which consists of a Plexiglass bar that seals the CR-39 onto cylindrical holes 1 ml each. This device allows to expose 4 CR-39 to 4 solutions each, for a total of 16 samples in one neutron irradiation. The irradiation position is at the end of the thermal column of the TRIGA Mark II reactor (close to its entrance), operating at 20kW for 30min [2], therefore samples receive a neutron fluence of $(10.4 \pm 0.4) \times 10^{10} cm^{-2}$ [18].

Irradiation

The following phases of the measurement after the preparation of samples are:

- Select the irradiation protocol, which depends on the type of information needed (imaging or quantification);
- Place the CR-39 in the Thermal Column. If it is the liquid device, detectors are already sealed in the Plexiglass bar; if samples are solid, CR-39 are arranged in a Plexiglass holder which keeps them vertical for irradiation;
- Add a reference sample, that can be a silicon wafer with a know superficial distribution of ^{10}B implanted and certified by NIST, or biological cell samples with known boron concentration previously prepared ([18]).
- Irradiate in the thermal column of the TRIGA Mark II

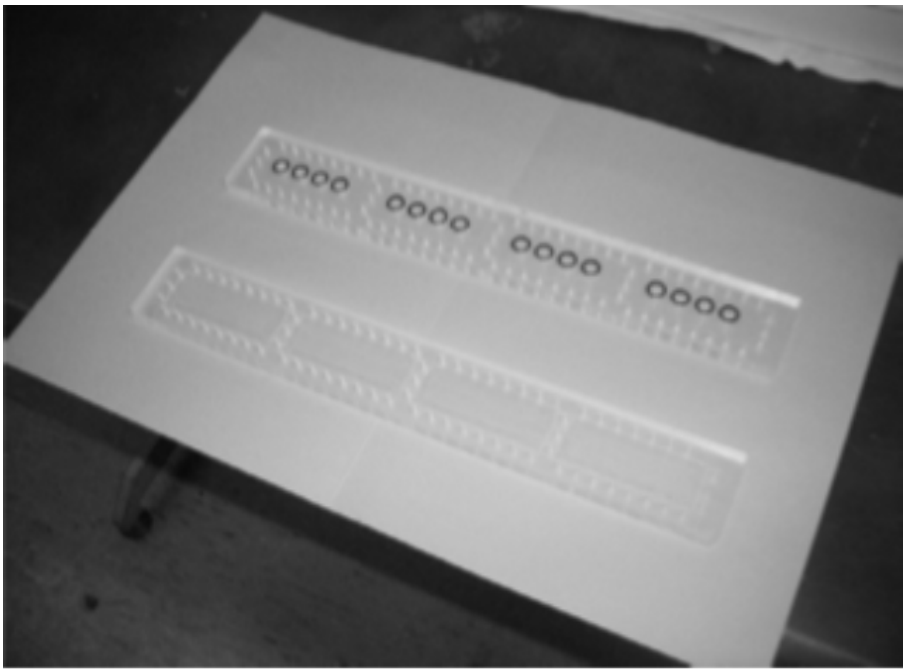

Figure 2.3: Liquid samples irradiation device. It is visible the inferior plexiglass bar with 4 housings for CR-39 slides and the superior bar with the sealed holes where the borated liquid solutions are poured.

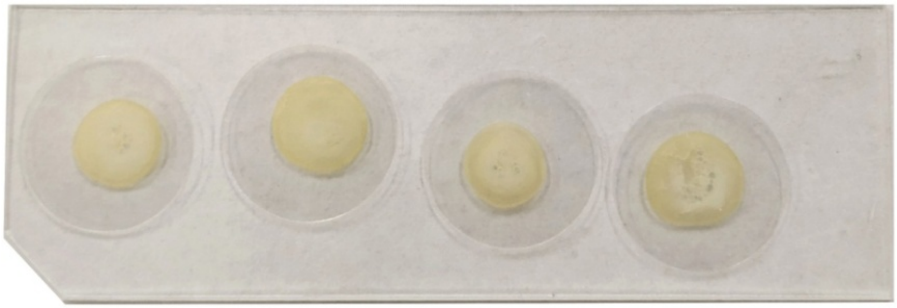

Figure 2.4: Solid sample positioned on a CR-39. For proper reference, the samples are numbered starting from the cut at the top right corner when the CR-39 is vertical.

2.1.3 Etching

After irradiation, the samples are removed from the CR-39. It is important to clean residual sample content from the detector surface. This can be performed with the following steps:

- Rinse the CR-39s with tap water to remove any loose debris or surface contaminants.
- Gently wipe the CR-39s with a soft, lint-free cloth or paper towel to remove any remaining residue. Avoid scratching the surface, which may introduce background

noise in the images or jeopardize the boron imaging.

For a correct etching procedure, the etching solution has to be prepared and brought to temperature, which requires 2 hours to have a stable temperature. The solution is heated and kept in a thermostatized chamber using water. There are two procedures to follow according to the type of irradiation:

- **Qualitative**: Irradiation at full reactor power (i.e. 250 kW for 2 hours) produce sample with overlapping tracks. These samples are etched with a 6.25M NaOH solution at 70°C for 20 minutes, see Table 2.1 for the protocol.
- **Quantitative**: Irradiation at low reactor power (i.e. 2 kW for 30 minutes) produce sample with low track density. For this case, the aim of the etching is to produce clear visible tracks that can be visualized by a microscope (blobs). For this protocol we use PEW40 solution at 70°C for 10 minutes, see Table 2.2 for the protocol.

Table 2.1: NaOH solution for 1 sample holder.

compounds	weight %	weight (g)
NaOH	20	37.5
H2O	80	150.0

Table 2.2: PEW40 solution for 1 sample holder.

compounds	weight %	weight (g)
KOH	0.15	22.5
C2H6O	0.40	60.0
H2O	0.45	67.5

After the etching the detector are rinsed with running tap water for about 1 minute, until the water runs clear and uniform over the CR-39 detector. For a better cleaning, the detectors are then positioned in another sample holder filled with distilled water to remove all the residuals. Finally, they are gently dried with paper cloth, avoiding scratching the surface.

2.1.4 Image Acquisition

The image acquisition is accomplished by combining together the Leica Microscope, the Prior stage and the ImagePro plus software installed on a Windows machine connected to the Leica Microscope camera and Prior motorized stage.

To turn on the microscope there are 2 switches, one to activate the light (on the back part of the base) and one to activate the body (on the back part of the vertical tower). Once the microscope is active it must be set into quantitative acquisition mode, which can be done by going to config > memory > 1 (from the microscope touch screen). Figure 2.6 shows the screenshot in the focus/Zoom tab once the qualitative image acquisition mode is activated. The next step is to set the light as shown in figure 2.7.

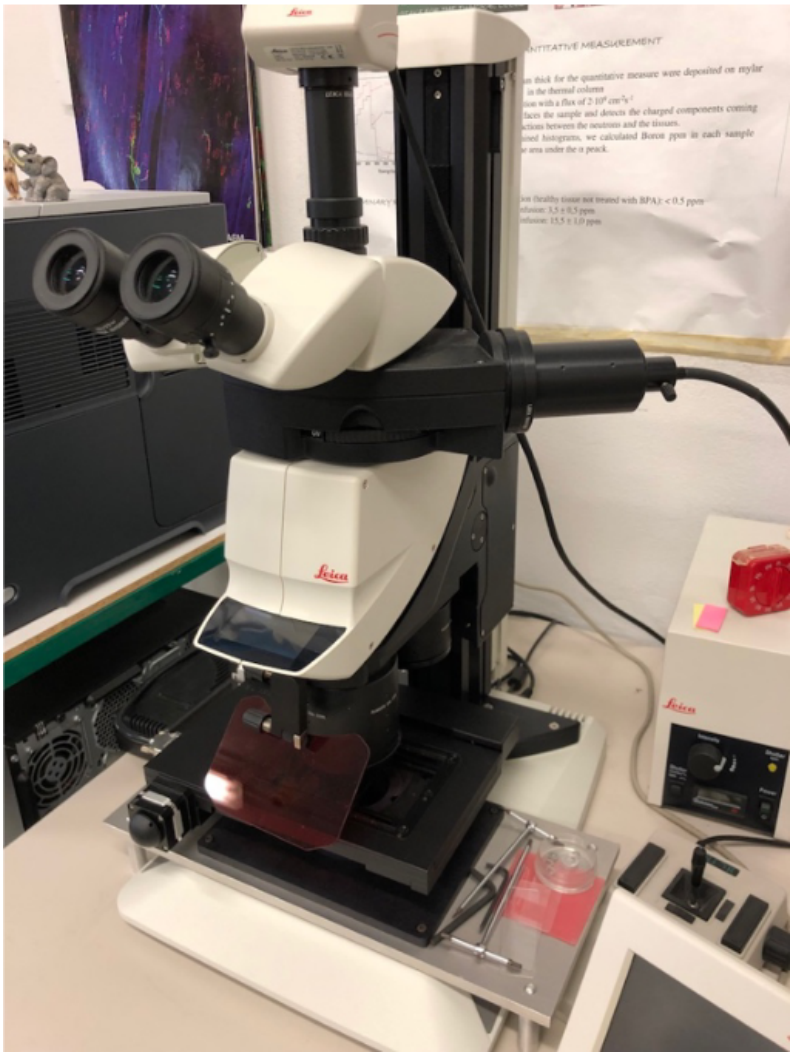

Figure 2.5: Leica Microscope with Prior OptiScan stage.

Once the microscope is up and running, the Prior OptiScan stage must be turned on (switch on the front panel of the stage). The next step is to start the ImagePro plus application, by running it as an administrator. When the application starts, the first thing to do is to calibrate the stage by clicking stage > stage-pro. It will require to bring the stage to its south-east position. Then the software will automatically calibrate the system. Next comes the activation of the camera, which can be trivially performed by clicking the camera symbol. At this point the camera is ready to take pictures. For quantitative measurements, in each sample on the CR-39 at least 40 random pictures must be taken all over the sample and stored in an appropriate directory.

When the images are acquired, they can be analyzed with a Python script. This will be covered in the next Chapter.

Figure 2.6: Focus/zoom settings for qualitative imaging

Figure 2.7: Light settings for qualitative imaging.

Image Acquisition In brief

- Turn the microscope on (2 switches)
  - Set microscope to configuration #1
- Turn the Prior stage on (1 switch);

- Open ImagePro plus:
  - Calibrate the stage
  - Open the camera application
  - Create a folder for the images
  - take 40 or more pictures
  - Launch the python script
  - Save the obtained mean track number information on a file.

In Chapter 3 the image analysis is described. This work is dedicated to the optimization of the algorithm and to the validation of the results by Monte Carlo, thus the samples used in the analysis are calibration samples with known boron concentration. These samples were previously generated by mixing cells obtained by liver tissue with a borated solution to obtain different boron concentration. The production and use of these samples is described in [18].

Chapter 3

Track counting algorithm and simulation

The first part of this Chapter will describe how the track counting algorithm works, then we will show and discuss the results obtained in an experiment. In the second part we will describe how we implemented and evaluated the results from a MC simulation with the Geant4 simulation toolkit [19]. This simulation was performed to count the total tracks that reach the CR39 from the irradiated sample. Comparing this number with the amount of tracks that we measure with the algorithm will give us an idea of the amount of tracks that we do not count because of the the algorithm or tracks that we loose during the etching.

3.1 The OpenCV library

To count the tracks from the neutron autoradiography samples we used the OpenCV Python library. OpenCV [20] is an open source library with different methods focused on image manipulation, object recognition and detection. We implemented some of its functions in the code both to modify the original images passed as arguments and to derive the boron concentration. In the following, we will describe the methods we used in our code one by one, specifying their scope in the code, how they work and what they do.

3.1.1 cv2.SimpleBlobDetector

This function represents the core of the algorithm. The goal of this function is to localize the blobs in an image. A *blob* is a group of pixels that share the same characteristic. In our case, it will be the pixel intensity. In fact, the tracks left by the α radiation on the CR-39 show a significant decrease in luminosity from the surrounding background and that is what differentiates them. This method operates on gray-scale images. For this reason, we need to read the original images passed as argument to our algorithm using a command to directly convert them into gray-scale ones (cv2.IMREAD_GRAYSCALE).

SimpleBlobDetector takes these images as an argument and converts them (one by one) into a binary image by applying a threshold with different reference values. It is possible to specify the maximum and minimum threshold to apply and the step for varying the reference value each time. Every pixel inside the image having intensity lower than the threshold is equalized to 0, otherwise its value becomes 1. It is not compulsory to delegate the image binarization to this function. Other methods can be used for the same purpose (we choose this second option), because they could be more appropriate for the kind of picture the algorithm is analyzing. Once the input image is binarized, the blob detector looks for those pixels whose neighbors share the same intensity. After a blob is localized, the detector can apply some filters based on our preferences. Calling the method cv2.SimpleBlobDetector_Params() it is possible to filter the blobs by their area (expressed in pixels), their circularity (Formula 3.1), their convexity (looks for indentations which are atypical for radiation induced tracks), minimum distance (blobs whose centers are below this distance will be merged into one) and color. By default, the blobDetector looks for dark spots on a white background (which is our case). However, it would be possible to search bright spots on a dark background too, by specifying it in the color parameter. After creating an instance of the detector with cv2.SimpleBlobDetector_create(params), we call the detect() method to localize the blobs [20].

$$\frac{4\pi Area}{Perimeter^2} \tag{3.1}$$

3.1.2 cv2.drawKeypoints()

This second function is used right after SimpleBlobDetector to show on an image the blobs found. Blobs obtained by analyzing an image are stored in an array as "keypoints". This array, which contains the coordinates of the center of each blob and its diameter, is passed as argument to drawKeypoints() along with other elements. In particular, the first parameter will be the source image (the one we used to find blobs), the second one is the fore-mentioned array containing the blobs. After that, we need to specify the characteristics of the blob we are drawing, such as color (BGR notation) and if we want to indicate their size too. The function drawKeypoints() will draw a circle around the blob or will indicate its center, following the specified parameter [20].

3.1.3 cv2.adaptiveThreshold()

As we anticipated, it is possible to bypass the threshold mechanism included in the SimpleBlobDetector, implementing it using another function. cv2.adaptiveThreshold() provides a more efficient way to binarize an image. A fixed and hard-coded value could not be appropriate if the image shows different lighting conditions in different areas. In these cases, a different variable value for threshold could be a better choice, depending on the region we are analyzing. The function takes different input parameters: the first one is the image we want to binarize (must be in gray scale); the second is the maximum value which is assigned to pixel intensity; after that, we need to specify which kind of

threshold we want to use. There are two choices: cv2.ADAPTIVE_THRESH_MEAN_C or cv2.ADAPTIVE_THRESH_GAUSSIAN_C. The first computes the threshold value by calculating an arithmetic mean among the pixels contained in the square whose side length is passed as an argument in the cv2.adaptiveThreshold() function minus a constant C; the second derives the mean by performing a weighted sum of the same area as before and subtracting C. The last two arguments passed when calling cv2.adaptiveThreshold are the block size, which defines the side of the square used by the threshold functions, and the value of C [20].

3.1.4 cv2.morphologyEx()

This function is used to reduce the normal noise present in a binarized photo. This function needs three parameters: the image on which perform the noising reduction; the type of the operation to perform and the kernel to use. A kernel is a square matrix whose dimension defines with how many surrounding pixels and the weights with whom to calculate the linear combination among pixels. The kernel runs along all the pixels in the photo, allowing to perform mathematical operations only on those selected pixels. The second parameter can be of five different types. However, just two of them are useful for our purpose: cv2.MORPH_CLOSE and cv2.MORPH_OPEN. The first performs a dilation followed by an erosion. Here, by dilation, we mean the process in which black pixels are converted to white ones if all the pixels under the same kernel area are not black. Erosion in the opposite process in which white pixels are turned black if not all pixels in the area defined by the kernel are white. These two processes are capable of eliminating small blobs derived from the threshold process or to smooth the contours of existing ones. In this way it will be easier for the blob detector to find them. cv2.MORPH_OPEN performs the same two operations in opposite order (erosion followed by dilation) [20].

3.2 Trace counting algorithm

The main objective of this dissertation was to develop an algorithm able to automatically count tracks generated on CR-39 plates by α radiation. We choose to build this algorithm in Python, due to its wide and detailed libraries. In particular we implemented some functionalities from the OpenCV library for the track count. As anticipated, the images we used are identical to the image 2.2 previously reported. For each tissue sample, 40 adjacent photos were taken as explained in the previous Chapter. The high number of photos we took per each sample is useful to avoid miscalculations of the concentration as a result of possible statistical fluctuation in the tracks number if observed on small groups of images. Ideally we could take images of the entire sample, this would be too time consuming especially when analyzing many irradiated samples. When analyzing new boron compounds, it is pivotal to evaluate the homogeneity of the boron distribution, higher homogeneity is correlated to a better compound. Thus, we can expect that the boron concentration may vary significantly, even within the same sample. This difference may be caused by various factors: poor boron uptake in some cells, poor compound distribution, different types of tissues in the same sample or just caused by the nature of the tumor tissue itself. Tumor grows irregularly, and some of its portions may be

well served by blood vessels, while others may not. In addition, some parts could even undergo necrosis. Being dead, necrotic tissue does not absorb boron from blood and this fact would result in a zero track count in the region of CR-39 that was in contact with that portion of tissue. It is important to correlate those regions with the correct tissue type through histological analysis, otherwise the measure would lead to a wrong concentration estimate. Taking into account all this information, we took the set of photos in the regions where the highest number of tracks was available. All these photos are collected in a "tif" format (the original format in which they are generated from the microscope camera), which appeared to be the best for track detection, while other more common formats did not allow for a correct count.

The first part of the algorithm is focused on image manipulation. In the following, the dedicated portion of the code is reported.

```
 for i in range(len(filelist)):
      Index = filelist.index(filelist[i])
      Index = Index + 1
      im = cv2.imread(path+'/'+filelist[i], cv2.IMREAD_GRAYSCALE)
      IntensityDistributionGraph(path+'/'+filelist[i], Index)
      im1 = cv2.adaptiveThreshold(im, 255, cv2.ADAPTIVE_THRESH_GAUSSIAN_C,
cv2.THRESH_BINARY, 301, 3)
      kernel = np.ones((2,2), np.uint8)
      im1 = cv2.morphologyEx(im1, cv2.MORPH_CLOSE, kernel)

      if ((Index - 1) % int(len(filelist)/3) == 1):
          plt.imshow(im1)
          plt.axis("off")
          plt.show()
          plt.close()
```

Figure 3.1: Image manipulation procedure

As anticipated, images are passed to the algorithm in "tif" format directly specifying the directory in which they are stored from command line. The algorithm enters the directory, sorting the files. After that, a loop over all the images is started. Being colored, the first step is to convert them in gray scale. This passage is necessary to obtain an image that the "detect" method of the cv2 library can analyze. Another requirement for the usage of this method would be to avoid colored blob detection (group of pixels having similar characteristics) on a black background. However, this is not our case, since the tracks are visible as dark spots on a clear back as we can observe in figure 2.2. Once an image is loaded and converted to gray scale, the first step is to apply the "adaptiveThreshold" method described in the previous section. In this way, we will be able to enhance the tracks' visibility against the background: if observed directly from the original photo, the tracks are blurry on their contours. That is because despite their darker appearance, they are not made of black pixels. A track is made up of pixels whose intensity is halfway between completely dark and bright ones. Applying a threshold algorithm, we can binarize the image, rounding to zero all the pixels whose intensities are lower than

the threshold value. With this precaution, the edges of the blobs become more neat, and their recognition against the background, now brighter, becomes easier. That is because the "detect" method analyzes the pixels intensities to find a group of pixels with a similar one, operating on binarized images. Eliminating all the blurry areas and equalizing all the values to zero facilitate this job. After this initial part, another passage is to apply the "morphologyEx" method to reduce the noise generated by the binarization procedure. In fact, even in the bright background there are some random pixels with lower intensities and they are brought to zero along with real tracks during binarization. This second step tries to remove them, or at least reduce their frequency and size, so that we will be able to filter them with the size parameter in the "SimpleBlobDetector" implementation. In figure 3.2 we can observe how the tracks become more evident after the application of the two mentioned methods. The image 3.2a will be the one in which the algorithm will perform the blob detection.

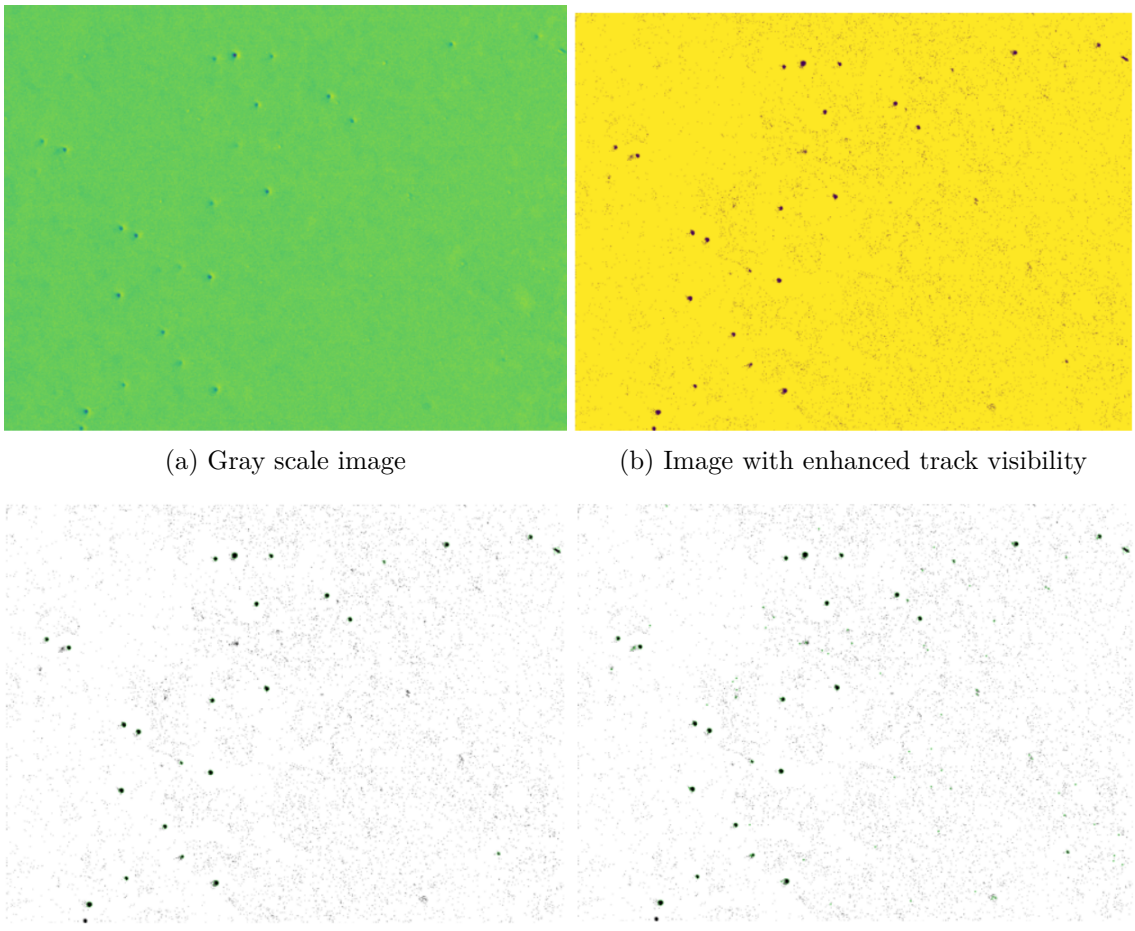

(a) Gray scale image

(b) Image with enhanced track visibility

(c) Blob detection with size constraint

(d) Blob detection without size constraint

Figure 3.2

The images are now ready for the blob detection. We create an instance of the SimpleBlobDetector, specifying the filters to apply to every blob detected. The most relevant one is the constraint that is placed on the size of the blobs. As anticipated, it is impossible to completely remove the noise from the binarized images. With this precaution, we are able to discard an extremely high number of false counts. It is common to have a greater number of false tracks than the true ones if such a countermeasure is not applied. We have a clear example of this fact in figures 3.2c and 3.2d. In the latter, we can see that the same photo generates tens of small blobs (marked in green) that do not correspond to a real track on the CR-39 plate. However, they can be easily discarded with a threshold on the minimum area allowed. All detected blobs are stored in an array (named "keypoints") with the coordinates of their center and their diameter. Image 3.2d show how method "drawKeypoints" takes this information and localize the blob on the binarized image with a green circle. The algorithm then saves a copy of the photo with the drawn blobs in a directory created at the beginning of the code run and add the number of blobs found in the last photo to the total count.

After this first part, when all the images in the directory have been analyzed, the algorithm invokes another file whose task is to look for artifacts in the images that can create anomalous detections (two arguments are passed to the function defined in this file: a tuple $(Index, len(keypoints), im\_with\_traces)$ and the total number of tracks identified. $Index$ represent the number identifying the image in the directory, $len(keypoints)$ is the number of blobs found in that image and im_with_traces is the image with the green circled tracks, similar to 3.2d). CR-39 detectors may have microscopic damages, dust, scratches or deformations. These could create a not-perfectly-smooth surface that during the binarization process create areas with vast dark portions or many small dark spots, which are identical, in size and appearance, to the tracks we are looking for. The blob detector is not able to distinguish between the two cases and considers them as tracks. In general, when such a case occurs, it does not generate a single extra blob (even if it was the case it would not affect the track count significantly), but many all grouped together, as in figure 3.3. The code calculates the mean value of the blob in a single image by dividing the total number of traces by the number of images. It also calculates the standard deviation and observes if some of the images present a number of traces which falls out the interval $\{mean - 2 * std; mean + 2 * std\}$. If that is the case, it shows the image to the user, asking if the image should be discarded or not.

The user directly enters the answer by typing Y, N or E, with two possibilities. If the number of the blobs is too high, as in the example provided by figure 3.3, the code ask to reject (Y), or accept (N) the photo, or to manually enter the number of blobs (E). If the photo is rejected, the code subtracts its number of tracks from the total count and adds the photo to the $rejectedImages$ list, otherwise, if the option E is chosen, the user has to manually insert the number of the tracks. Differently, if the photo shows too few tracks the user must say if the tracks are correctly identified (Y or N), in the case they are not the user is asked to enter the number of tracks manually, with 0 used to discard the image (in this eventuality the images will be again added to the $rejectedImages$ list and its number of blobs will be subtracted by the total, while if a number is passed

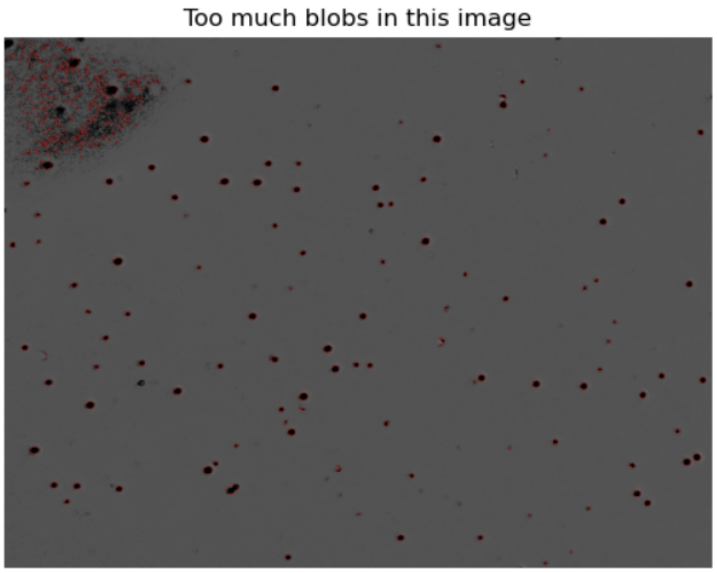

Figure 3.3: Anomalies arised from binarization in binary images are visible in the upper-left corner of the image

as argument this new value will substitute the older one previously calculated). After all this, the function returns the list of the rejected images, and the adjusted total blob count.

Once this operation is complete, the algorithm returns to the main file and calculates the perimeters and areas of the tracks using the diameter of the blobs obtained by the blob detector and previously stored in the "keypoints" array. All the results are then added to two different lists: "blobAreas" and "blobPerimeters". Another module will make use of these two arrays to plot the distributions of both areas and perimeters. The files thus produced will be saved in the "Graphs" directory, which was previously built by the algorithm itself. The same module also plots, for each image (before binarization), the intensity distribution of the pixels and stores these graphs in the same directory along with the plot of areas and perimeters.

After that, the calibration module is called. The main file passes the directory containing the calibration images and the corresponding boron concentrations to the calibration file. The calibration image set contains 40 images for each sample (4). For everyone of them, the algorithm applies the same procedure already described for the first set of images (conversion to gray scale, threshold and binarization). After every 40 images the calibration file calculates the mean number of tracks revealed per image and their standard deviation. Similarly to what happened in the first case, it also calls the file that looks for anomalies in the various images and asks the user if it is necessary to exclude the ones showing irregular blob counts from the total. After that, the algorithm plots the points having the boron concentration as X coordinate and the mean counted traces

as Y, with their errors obtained considering that the track counting process follows a Poisson distribution, the 3σ error is computed by using this formula:

$$E = 3\frac{\sqrt{\text{Total number Of Tracks}}}{\text{Nuber Of Images}} \tag{3.2}$$

Then, the linear fit of these points is performed using the ODR (Orthogonal distance regression) algorithm of the "scipy" library and we can observe in figure 3.4.

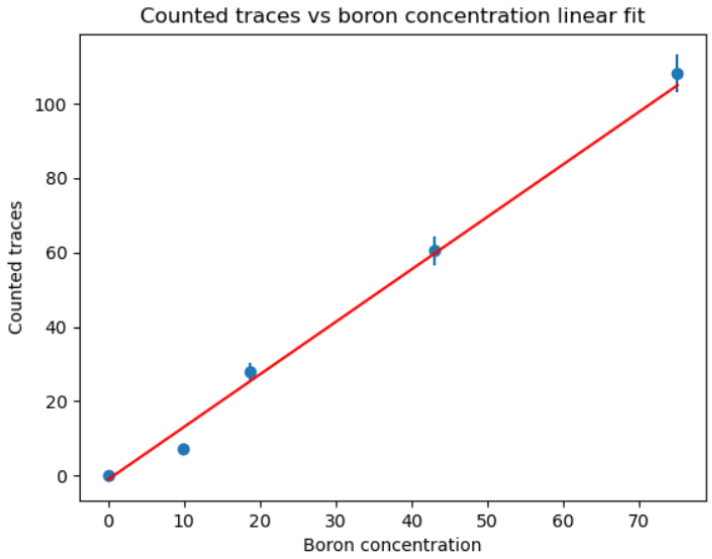

Figure 3.4: Linear fit of the counted tracks vs the boron concentration. The error bars represent a 3σ interval.

From this fit, the algorithm extracts the slope of the line and returns it to the main file. After that, the mean number of tracks is printed with the corresponding boron concentration and the plot is saved in the "Graphs" directory. The main file checks the slope value: if it was 0 it would mean that there was no correlation between boron concentration and tracks counted. This case and the eventuality of a negative slope must be rejected. In these cases, an error message will warn the user of the failed calibration. If the slope is greater than zero, the algorithm calculates the mean number of tracks per image by dividing the adjusted value of total tracks (the one returned after the check to find anomalies) by the total number of images analyzed minus the number of rejected images (the ones discarded for having anomalous counts). This result will be divided by the slope, thus obtaining the boron concentration in the analyzed sample.

The full code of the algorithm is available in a public gitHub repository [21].

3.3 The Geant4 simulation

Along with the counting algorithm, we developed a simulation, using the Geant4 simulation toolkit [22, 23, 24], the aim is to understand how many tracks we are actually counting with respect to the tracks that reach the detector. Geant4 is a software package, written in $C++$, which can be used to simulate the passage of particles through matter and how they interact with it. With Geant4 we are able to describe a geometry that replicates a real world scenario, both in shape and materials. Elementary particles are already included in the software, along with detailed physics models for particle-matter interaction. This software is able to store information about many different physical quantities, such as: particle energy, momentum, position, energy and momentum variations between two consecutive interactions and more. Geant4 provides different base classes that the user have to implement. There are some classes whose implementation is compulsory to obtain a working simulation, while others are optional. The compulsory classes are: G4VUserDetectorConstructor, G4VUserPhysicsList, G4VUserActionInitialisation and G4VUserPrimaryGeneratorAction. The first one is the class we need to implement in order to define the materials and geometry used in our experiment. This class possesses only one virtual method that returns the pointer to the world volume, which is the largest volume in the simulation, the one that contains all other smaller volumes. In our case, these smaller volumes will be the CR-39 and the tissue sample, as we will show later in more detail. G4VUserPhysicsList defines the models to be used in the simulation. The user could define his/her own particles and the most suitable physical processes. However, Geant4 has some ready-to-use physics lists that could simplify this part. G4VUserPrimaryGeneratorAction is the class delegated to particle production. It also contains a purely virtual method (void GeneratePrimaries(G4Event*)=0) that must be implemented, which is called in loop by the RunManager (the file responsible for handling the simulation) during the simulation so that primary particles can be generated one at a time. The last class, G4VUserActionInitialization, also contains a mandatory pure virtual method. In this case, this class will instantiate all user action objects (mandatory or not). In particular, via this class, we can call all the optional classes that allow us to extract particles information during or after the simulation. These classes are G4UserRunAction, G4UserSteppingAction, G4UserEventAction, G4UserStackingAction and G4UserTrackingAction.

The first part of this simulation is focused on the construction of a simplified geometry that could simulate the α radiation emitting tissue in contact with the CR-39 detector. The description of the geometry spans from volumes definition to material composition. For our purpose, the definition of just three materials (air, tissue and CR-39) was enough. We started by manually defining five elements (hydrogen, oxygen, carbon, nitrogen and argon), which represent the vast majority of the components in the structures we are simulating. All the materials where defined with direct reference to the Geant4 class G4Material. We defined the air as a compound of nitrogen(78%), oxygen (21%) and argon (1%) with a density of 1.225 kg/m^3. The tissue is composed of four elements, as suggested in the ICRU reports [25]. O, C, H, N are present as 76.2%, 11.1%, 10.1% and 2.6% of the total mass respectively. In the same file we define all the volumes required

to represent our system. We need a bigger parallelepiped that contains the other two smaller objects. In this case a box of $12 \cdot 12 \cdot 2$ cm^3 is enough. The empty space in this volume, which is not occupied by the other two smaller volumes, is filled with air. The remaining volumes must represent the CR-39 detector and the tissue sample, with their respective materials. The former is built as another box ($1 \cdot 10 \cdot 0.1$ cm^3), while the shape of the tissue sample is well approximated using a small cylinder leaned on the top of the detector (radius equals to 0.5 cm and height of 0.01 cm).

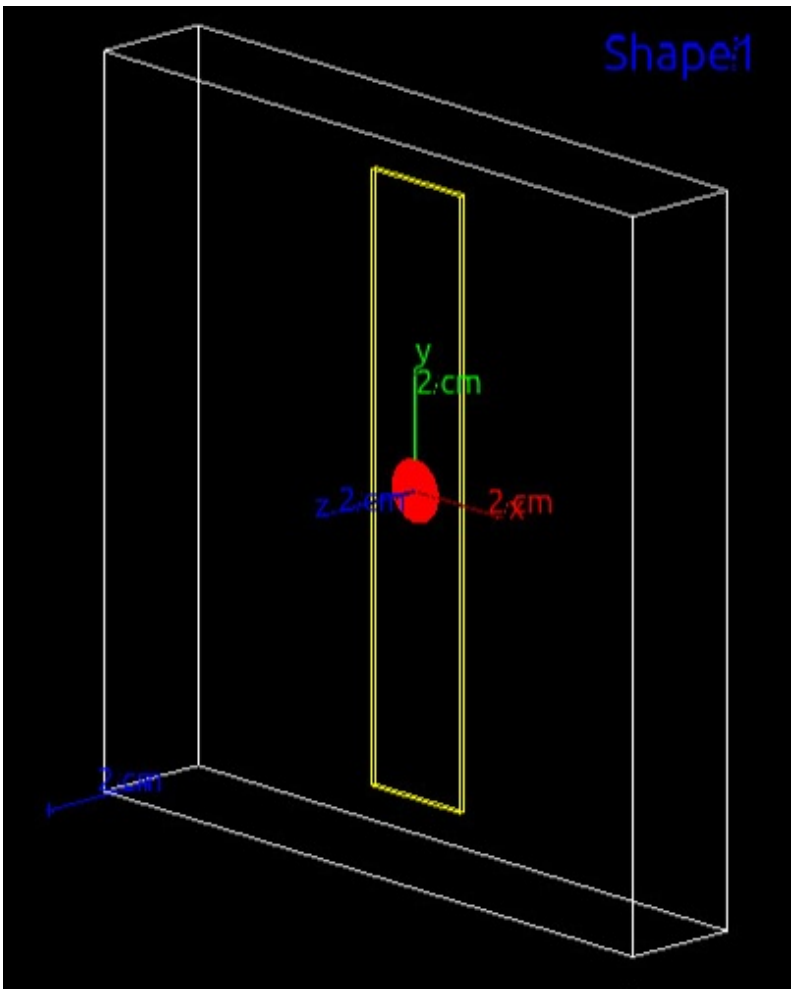

Figure 3.5: Visualization of the geometry setup in our simulation.

In figure 3.5 we can observe our three volumes. The biggest white box is the world volume (contains air), the detector (CR-39) is shown as yellow, while the tissue sample is red. In BNCT an external neutron flux penetrates the tissue, encounters a boron nucleus and, thanks to the capture process, releases an α particle and a Li nucleus. In our simulation we decided to generate both α and Li particles, but separately in four different simulations. We transported both of them twice, varying the particle energy, with each simulation containing 10^6 particles. In the case of α particles the two simulation

were run with energies of 1.5 and 1.8 MeV respectively, while the energies were 0.8 and 1 MeV, in the case of lithium nuclei. In every case, the particles were uniformly generated in the tissue volume with an isotropic direction of propagation. The choice of running two different simulations is justified by the fact that, as we described at the beginning of the first chapter, the vast majority (94 %) of the α particles Li nuclei, produced during the neutron capture by the boron nuclei, have lower energy (1.5 for α and 0.8 for Li). Just a smaller portion will be generated with greater energy. In Geant4 there are different possibilities to define a radiation source. In our case, we decided to use a macro file, which is a text file passed as argument when the simulation is run. The advantage of this configuration is that we do not need to recompile the code if we want to change some characteristics of the source. We just need to pass another macro or to modify the existing one.

In figures 3.6a and 3.6b we can observe the representation of the particles run by the code (blue/yellow lines). Here, the tissue sample is colored in red, while the CR-39 plate is yellow. As we can clearly see, some of them escaped the tissue sample in a direction opposite to the CR-39 plate. Those particles will not be revealed, along with the few ones emitted in parallel to the detector and the ones absorbed within the tissue itself. As anticipated, we performed four different simulations, running 10^6 particles each time. In the table below, we can observe the number of interactions obtained between the different particles, at different energies, with the CR-39 plate.

	α (1.5 MeV)	α (1.8 MeV)	Li (0.8 MeV)	Li (1 MeV)
interactions	91737	111776	36331	37444

Table 3.1: Results of number of particles reaching the CR-39 surface when simulating 10^6 randomly generated primary particles within the tissue volume.

These quantities allow us to derive the geometrical efficiency of our system by dividing the total number of interactions ($\alpha + Li$ with low energies or with high energies separately) by 10^6 and by performing a weighted mean of the two results. If we multiply the coefficient obtained from this calculation with the number of expected reactions inside the tissue samples, we should have an estimation of the number of tracks we should expect in the images used for our trace counting algorithm. In fact, we can obtain the reaction rate using the formula:

$$\Psi = \frac{V d \phi N_A \sigma M_f}{A} \tag{3.3}$$

Here, V represents the volume of tissue subtended to a single microscope image (the ones used in the algorithm), d is the tissue density (we considered it as equal to the water density), ϕ is the neutron fluence, M_f is the fraction of mass made of ^{10}B, with A its number of mass, σ the cross section for the capture reaction (4000 barn) and N_A the Avogadro's number. From this equation, supposing a concentration of 10 ppm of ^{10}B, we estimated a total number of reactions of around 350 per area of image. Not all the particles released in these reactions will be able to reach the CR-39. Many of them will

be absorbed within the tissue and other will propagate in a direction opposite to the detector. This effect is took into account by our Geant4 simulation. The product of the geometrical efficiency and this last value (350) returns an expected track count of around 45, which is far way higher than the value obtained with the algorithm. In the following, we report the estimation performed for the number of reactions in the case we had a boron concentration of 70 ppm. Starting from equation 3.3 we have:

$$\Psi = \frac{72 \cdot 10^{-18} m^3 \cdot 10^3 kg/m^3 \cdot 2 \cdot 10^{14} n/s \cdot m^2 \cdot 6.022 \cdot 10^{23} mol^{-1} \cdot 4 \cdot 10^{-25} m^2 \cdot 7 \cdot 10^{-5}}{10} \tag{3.4}$$

that brings to the value of 2450. If we multiplied this value by the geometrical efficiency (0.13) we would obtain 318, which is the expected value of tracks for a boron concentration of 70 ppm. Again, the counted value is lower than the expected one. In fact, our algorithm only revealed a mean value of 108 tracks per images provided.

The full code of the simulation is available in a public GitHub repository as indicated in the reference. [26].

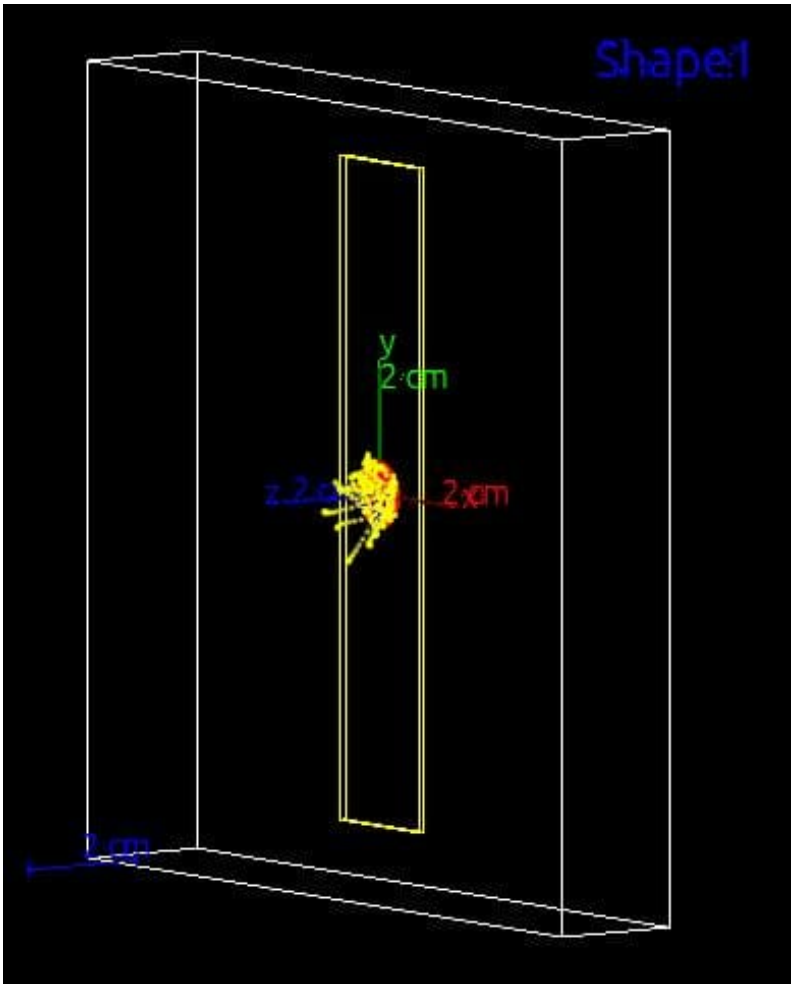

(a) View of the graphic representation of the trajectory traveled by the α particles.

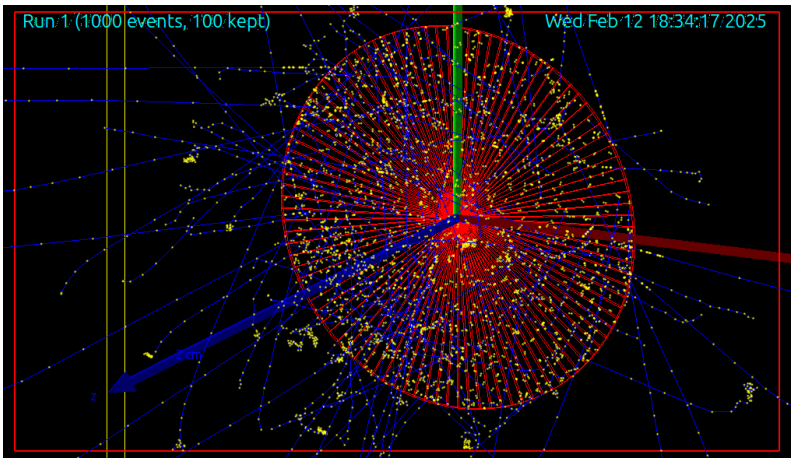

(b) Close view of the graphic representation of the trajectory traveled by the α particles.

Chapter 4

Conclusions

This thesis focused on developing a methodology to evaluate boron concentration in biological samples for Boron Neutron Capture Therapy (BNCT). The primary objectives were to implement an automated track-counting algorithm using OpenCV to analyze CR-39 solid-state nuclear track detectors and to develop a Monte Carlo simulation with Geant4 to assess geometric efficiency. These tools provide a more accurate and efficient approach to measuring boron distribution and concentration, which is crucial for optimizing BNCT drug delivery. The main result of this work is the achievement of a

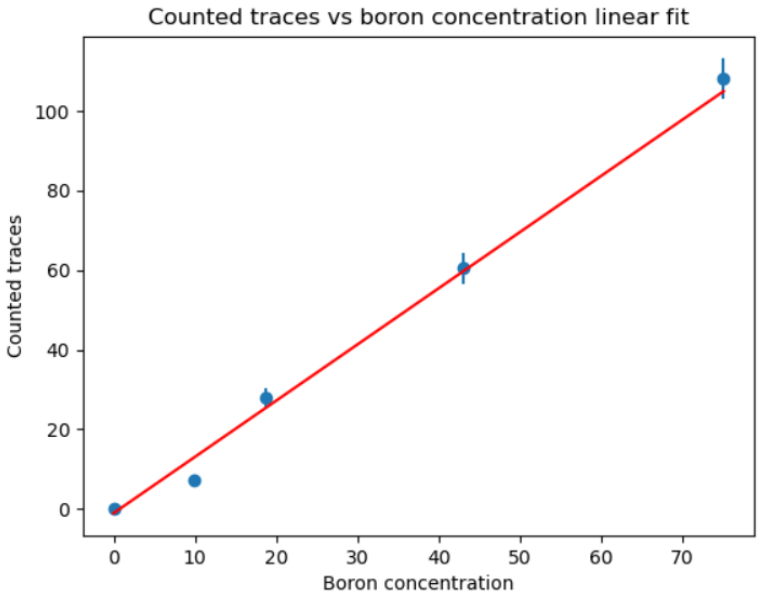

calibration curve (the red line reported in the figure above, with slope $m = 1.41$) that correlates a certain amount of counted tracks to boron concentration within the tissue sample ($tracks = 1.41 \cdot concentration$). The automated track-counting algorithm significantly improved the precision and reproducibility of boron concentration measurements,

while the Monte Carlo simulation provided valuable insights into the geometric efficiency of particle detection. By correlating experimental data with simulation results, we established a robust framework for evaluating new boron-containing compounds in preclinical studies.

Further work will be performed to understand why we loose many tracks during the counting process. As we showed in Chapter 3, with equation 3.3 and the geometrical efficiency, we would expect a higher track count than the one obtained. Such a low number observed (we expect to lose around 66% of the total tracks, considering the values obtained for the sample with 70 ppm of boron) could have more than a single cause. A possible explanation could be that the etching procedure removes the more shallow tracks (the ones generated by particles with less energy and the ones caused by non perpendicular hits). More analysis are needed to clarify this aspect, in order to achieve a better track counting in the future.

The work presented in this thesis will contribute to an upcoming scientific publication. Additionally, this technique will be employed in future studies to assess novel boron formulations, aiding in the development of more effective compounds for BNCT applications. These advancements will help enhance the selectivity and efficacy of BNCT, ultimately improving treatment outcomes for patients.

Bibliography

[1] Agustina Mariana Portu et al. “Enhanced Resolution of Neutron Autoradiography with UV-C Sensitization to Study Boron Microdistribution in Animal Models”. In: *Life* 13.7 (2023), p. 1578.

[2] Ian Postuma et al. “An improved neutron autoradiography set-up for B concentration measurements in biological samples”. In: *Reports of Practical Oncology and Radiotherapy* 21.2 (2016), pp. 123–128.

[3] Ana Mailén Dattoli Viegas et al. “Detailed dosimetry calculation for in-vitro experiments and its impact on clinical BNCT”. In: *Physica Medica* 89 (2021). Cited by: 4, pp. 282–292. DOI: 10.1016/j.ejmp.2021.08.010. URL: https://www.scopus.com/inward/record.uri?eid=2-s2.0-85114042359&doi=10.1016%2fj.ejmp.2021.08.010&partnerID=40&md5=ca96b979c99844ddea25326691277808.

[4] Eric J Hall, Amato J Giaccia, et al. *Radiobiology for the Radiologist*. Vol. 6. Philadelphia, 2006.

[5] Frank Herbert Attix. *Introduction to radiological physics and radiation dosimetry*. John Wiley & Sons, 2008.

[6] IAEA ICRU. “Relative biological effectiveness in ion beam therapy”. In: *IAEA Tech Reports* 461 (2008), pp. 1–165.

[7] Jack Valentin. “Relative biological effectiveness (RBE), quality factor (Q), and radiation weighting factor (wR): ICRP Publication 92”. In: *Annals of the ICRP* 33.4 (2003), pp. 1–121.

[8] W Friedland et al. “Comprehensive track-structure based evaluation of DNA damage by light ions from radiotherapy-relevant energies down to stopping”. In: *Scientific reports* 7.1 (2017), p. 45161.

[9] INTERNATIONAL ATOMIC ENERGY AGENCY. “Neutron monitoring for radiation protection / International Atomic Energy Agency”. In: (Oct. 2023).

[10] KOREA ATOMIC ENERGY RESEARCH INSTITUTE. “Table of nuclides”. In: (2005). URL: www.atom.kaeri.re.kr.

[11] MD Bethesda. “International Commission on Radiation Units and Measurements, Clinical Neutron Dosimetry-Part I: Determination of Absorbed Dose in a Patient Treated by External Beams of Fast Neutrons”. In: *Journal of the ICRU* (1989).

[12] *Current Status of Neutron Capture Therapy*. TECDOC Series 1223. Vienna: INTERNATIONAL ATOMIC ENERGY AGENCY, 2001. URL: https://www.iaea.org/publications/6168/current-status-of-neutron-capture-therapy.

[13] AA.VV. “Methods and models of dose calculation”. In: *IAEA TecDoc on BNCT, under publication* ().

[14] Horst Liskien and Arno Paulsen. “Neutron production cross sections and energies for the reactions 7Li (p, n) 7Be and 7Li (p, n) 7Be*”. In: *Atomic data and nuclear data tables* 15.1 (1975), pp. 57–84.

[15] *Advances in Boron Neutron Capture Therapy*. Non-serial Publications. Vienna: INTERNATIONAL ATOMIC ENERGY AGENCY, 2023. ISBN: 978-92-0-132723-9. URL: https://www.iaea.org/publications/15339/advances-in-boron-neutron-capture-therapy.

[16] Huifang He et al. “The basis and advances in clinical application of boron neutron capture therapy”. In: *Radiation Oncology* 16 (2021), pp. 1–8.

[17] Hiroaki Kumada, Takeji Sakae, and Hideyuki Sakurai. “Current development status of accelerator-based neutron source for boron neutron capture therapy”. In: *EPJ Techniques and Instrumentation* 10.1 (2023), p. 18.

[18] MA Gadan et al. “Set-up and calibration of a method to measure 10B concentration in biological samples by neutron autoradiography”. In: *Nuclear Instruments and Methods in Physics Research Section B: Beam Interactions with Materials and Atoms* 274 (2012), pp. 51–56.

[19] Stefano Agostinelli et al. “GEANT4-a simulation toolkit”. In: *Nuclear Instruments and Methods in Physics Research Section A Accelerators Spectrometers Detectors and Associated Equipment* 506 (July 2003), p. 250. DOI: 10.1016/S0168-9002(03)01368-8.

[20] G. Brandski. “The OpenCV Library”. In: *Dr. Dobb’s Journal of Software Tools* (2000).

[21] I. Postuma and S. El Bouadli. “Track counting algorithm in BNCT”. In: (2025). URL: https://github.com/19sam96-git/countingAlgorithm.

[22] John Allison et al. “Recent developments in Geant4”. In: *Nuclear instruments and methods in physics research section A: Accelerators, Spectrometers, Detectors and Associated Equipment* 835 (2016), pp. 186–225.

[23] John Allison et al. “Geant4 developments and applications”. In: *IEEE Transactions on nuclear science* 53.1 (2006), pp. 270–278.

[24] Sea Agostinelli et al. “GEANT4—a simulation toolkit”. In: *Nuclear instruments and methods in physics research section A: Accelerators, Spectrometers, Detectors and Associated Equipment* 506.3 (2003), pp. 250–303.

[25] International Commission on Radiation Units and MD (United States) Measurements Bethesda. *Tissue substitutes in radiation dosimetry and measurement*. Jan. 2025.

[26] I. Postuma and S. El Bouadli. “Geant4 simulation of alpha particles hitting on CR39”. In: (2025). URL: https://github.com/19sam96-git/CR39_sim/tree/master.